TUFTS UNIVERSITY

DOE/ER/40702-9
Tufts University
May 2, 1995

A cross section measurement of charm hyperons Ξ_c^+ and Ξ_c^0 in 250 GeV p/K/π-nucleon interactions

Juan Francisco
Astorga Vergara

(Ph.D. Thesis – Tufts University)

U.S. DEPARTMENT OF ENERGY
GRANT
DE-FG02-92 ER40702

May, 2 1995

DISCLAIMER

DISCLAIMER

Portions of this document may be illegible in electronic image products. Images are produced from the best available original document.

A cross section measurement of charm hyperons Ξ_c^+ and Ξ_c^0 in 250 GeV p/K/π-nucleon interactions

A dissertation

submitted by

Juan Francisco

Astorga Vergara

In partial fulfillment of the requirements

for the degree of

Doctor of Philosophy

in

Physics

TUFTS UNIVERSITY

May, 1995

Adviser: Austin Napier

ABSTRACT OF THE DISSERTATION

A cross section measurement of charm hyperons Ξ_c^+ and Ξ_c^0 in 250 GeV p/K/π-nucleon interactions

by Juan Francisco

Astorga Vergara, Ph.D.

Dissertation Director: Austin Napier

Fermilab Experiment 769 used a charge-selected, hadron beam of mean energy 250 GeV/c, composed of pions, kaons, and protons, impinging on beryllium, aluminum, copper and tungsten targets. Using a sample of approximately 4000 $\Xi_s^- \to \Lambda^0\pi^-$ decays, measurements of the charm baryon forward cross sections times branching ratio $\pi^\pm N \to \Xi_c^+ X$ and $\pi^\pm N \to \Xi_c^0 X$ are presented. Upper limits on $\sigma \times BR$ are also determined for the states $\Xi_c^+ \to \Xi_s^-\pi^+\pi^+$ and $\Xi_c^0 \to \Xi_s^-\pi^+$ produced in (p, π^+, π^-, K^+, K^+)-nucleon interactions.

The E769 Collaboration

G.A. Alves,[1] S. Amato,[1] J.C. Anjos,[1] J.A. Appel,[2] J. Astorga,[5]
S.B. Bracker,[4] L.M. Cremaldi,[3] C.L. Darling,[7] R.L. Dixon,[2] D. Errede,[6]
C. Gay,[4] D.R. Green,[2] R. Jedicke,[4] P.E. Karchin,[7] S. Kwan,[2] L.H. Lueking,[2]
J.R.T. de Mello Neto,[1] J. Metheny,[5] R.H. Milburn,[5] J.M. de Miranda,[1]
H. da Motta Filho,[1] A. Napier,[5] D. Passmore,[5] A. Rafatian,[3] A.C. dos Reis,[1]
W.R. Ross,[7] A.F.S. Santoro,[1] M. Sheaff,[6] M.H.G. Souza,[1] W.J. Spalding,[2]
C. Stoughton,[2] M.E. Streetman,[2] D.J. Summers,[3] S.F. Takach,[7] A. Wallace,[7] and
Z. Wu[7]

[1] *Centro Brasileiro de Pesquisas Físicas, Rio de Janeiro, Brazil*
[2] *Fermi National Accelerator Laboratory, Batavia, IL 60510*
[3] *University of Mississippi, University, MS 38677*
[4] *University of Toronto, Toronto, Ontario, Canada, M5S 1A7*
[5] *Tufts University, Medford, MA 02155*
[6] *University of Wisconsin, Madison, WI 53706*
[7] *Yale University, New Haven, CT 06511*

Acknowledgements

A long time ago and in a different part of the world these two students decided to come to the US and see if they could make it into the Ph. D. program. I must begin then by saying thanks to William Leeson for taking that trip with me. I thank Sergio del Campo and Miguel Villanueva for their initial support and having ready an apartment where to live. I also thank my parents for overcoming the *latino* family attachment and understanding when I had to go.

Foremost, I thank Marolí Ixic for her support throughout this process. She waited patiently the first three years and not so patiently the last two *this coming May*.

I thank Austin Napier for his continuous support and encouragement. He introduced me to experimental physics and opened a door to a fascinating world. I also thank him for introducing me to UNIX and for the fun times while *fixing* hardware stuff.

I owe special thanks to Paul Karchin who has helped me in more than one occasion with this project. His honest criticism has been invaluable to finish this work.

I thank Jeff Appel for all the help he gave me to conduct this project. His encouragement to finish this study has been a powerful incentive. When I realized the size of the charm baryon signal I was afraid that there was no hope to publish any of it, he quickly went to his desk dug some papers on the matter and showed me that it was possible. I also thank Jeff for loading tapes for the Monte Carlo generation.

Without the help of Dave Passmore this project would have taken a lot longer.

In a great gesture, he gave me the Lambda code to start the hyperon study. He also developed the code for the analysis of cuts, that helped me to extract the strange cascades of our data.

Andrew Wallace helped with the trigger corrections and the beam count has been invaluable for this project. I thank him for that and for helping me to calm down when I was very nervous in an APS meeting.

I thank all the members of my thesis committee, Drs. Austin Napier, Richard Milburn, Gary Goldstein from Tufts and Paul Karchin from Yale University.

Table of Contents

List of Tables

List of Figures

Chapter 1
Hadronic Production of Charm Hyperons

The study of the elemental constituents of the Universe has always been of particular interest and fascination. The first model ever proposed was introduced about 25 centuries ago by Anaximenes of Miletus. The latest, developed originally by Gell-Mann, Zweig and others between 1960-1970[1, 2], proposed a universe composed of quarks, leptons and gauge bosons to mediate interactions between them. Originally there were three quarks, *up, down, strange* but later and for various reasons a fourth quark, *charm*, was introduced. By now, the total number of quarks is six, the remaining two are: *beauty* and the newly discovered *top*.

Experimentally, the charm quark was found independently by Richter and Ting in 1974 with the J/ψ meson. This was 20 years ago! Since then considerable progress has been made in the study of charm meson spectroscopy. J/ψ, D^0, D^+ and resonant state properties are known with reasonable precision. Some of the latest charm meson experiments at Fermilab and CERN expect signal sizes of the order of several tens of thousands.

Charm baryon spectroscopy, on the other, hand presents a completely different scenario, and after 20 years of the discovery of the J/ψ the lifetime of Ξ_c^+ baryon is only known within 20% statistical errors!

The lack of high statistics experiments on charm baryon spectroscopy leaves the charm baryon hadroproduction process poorly understood. Except for Λ_c^+, cross section measurements are nearly non-existent. So are measurements of atomic mass dependence and the leading particle effect seen in D mesons.

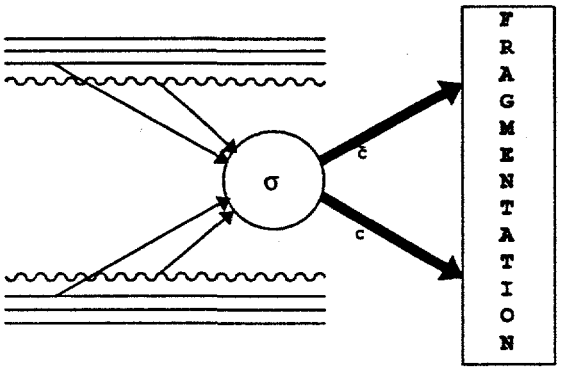

Figure 1.1: Kinematics of collision process.

1.1 Charm Cross Section

Quarks are now established as the fundamental constituents of strongly interacting particles. The search for a dynamic theory of quark interactions has led to the development of Quantum Chromodynamics. In principle, the hadron-hadron cross section must be calculated within the framework of QCD. Figure 1.1 represents the basic hadroproduction process as is understood in such a framework.

Three basic components must be included in the cross section, namely:

- The hard parton cross section, $\hat{\sigma}$, of the initial hadrons.
- The parton, quark and gluon, distribution of incident hadrons.
- The hadronization of charm quarks into charm particles.

The cross section is then written as[3]:

$$\sigma = \sum_{ij} \int dx_1 dx_2 f_i(x_1, \mu) f_j(x_2, \mu) \hat{\sigma}(x_1 x_2 s, \mu^2),$$

where;

- $f_{i,j}$ are the distribution of partons of the incident hadrons, also called the Structure Functions.

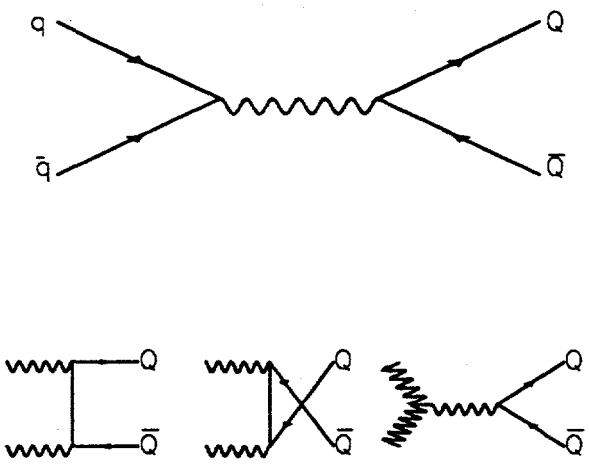

Figure 1.2: Second order (leading order) QCD Feynman diagrams for heavy hadronic quark production.

- $x_{1,2}$ are the momentum fractions carried by the partons and evaluated at a scale μ
- s is the square of total center of mass energy of the incident hadrons.

1.1.1 Hard Parton Cross Section

The parton-parton cross section is the only part of the total cross section that is calculable by perturbative techniques. The second order calculations have been done by several authors[4]-[6]. At this order, there are 2 main contributions to the cross section, namely: gluon-gluon fusion and quark-antiquark annihilation,

$$g + g \rightarrow Q + \bar{Q}$$
$$q + \bar{q} \rightarrow Q + \bar{Q}.$$

Figure 1.2 shows the Feynman diagrams contributing to lowest order cross section.

Third order cross section calculations have been carried out by Nason, Dawson & Ellis[7] and more recently by Beenakker, *et al.*[8]. The new calculation includes

many other different Feynman diagrams whose main feature is the emission of virtual and real gluons.

The main consequence of these third order calculations are that: the total cross section $\hat{\sigma}$ increases for a factor of $\sim$3 relative to that of lower order, the differential cross section shape does not change significantly and finally, in the E769 energy regime, 95% of the total cross section is due to the gluon-gluon fusion subprocess.

1.1.2 Parton Structure Functions

Structure functions are necessary in order to calculate the hard parton subprocess cross sections. These functions come from experimental data. Most measurements are related to quark structure functions for nucleons, pions and kaons[9], while their gluon counter parts are poorly known.

1.1.3 Hadronization

Structure functions, $f_{i,j}(x_{1,2}, \mu)$, and the hard parton cross section, $\hat{\sigma}$, are used to calculate the total $c - \bar{c}$ cross section. In reality, experiments measure cross sections for final particle states. Hadronization requires non-perturbative calculations and therefore are usually treated with Monte Carlo techniques.

1.2 Other Experiments

As stated above, the study of charm baryon production does lack basic measurements. Up to now, CERN-NA32 is the only experiment measuring cross sections[10], and the most accurate mean life measurement comes from FERMILAB E687[11], a photo-production experiment. Cross section data are shown in Table 1.1. NA32 has also run with K^- beam and has found a few charm events but has not reported a cross sections for them, except for 7 Λ_c events, all of them anti-baryons.

Hyperon	Events	$\sigma \times$ B μb/nucleon
$\Lambda_c^+ \to pK^-\pi^+$	154	$0.18 \pm 0.02 \pm 0.03$
$\Xi_c^0 \to pK^-\bar{K}^*(892)$	3	$0.019 \pm 0.011^{+0.066}_{-0.009}$
$\Xi_c^+ \to \Xi_s^-\pi^+\pi^+$	3	$0.13 \pm 0.08^{+0.07}_{-0.05}$

Table 1.1: **NA32** cross section data. These data have been taken with a 230 GeV π^- beam. The errors quoted are statistical (first) and systematic (second).

Hyperon	Events	$\sigma \times$ B/nucleon
Λ_c	7	$0.16 \pm 0.06 \pm 0.04$
Ξ_c^0	1	
Ξ_c^+	1	

Table 1.2: **NA32** data. These data have been taken with a 230 GeV K^- beam. The errors quoted are statistical (first) and systematic (second).

Hyperon	Events	Lifetime in ps
Ξ_c^0	42	$0.101^{+0.017}_{-0.025} \pm 0.005$
Ξ_c^+	30	$0.41^{+0.08}_{-0.11} \pm 0.02$

Table 1.3: **E687** Mean life data. This experiment ran with a 220 GeV photon beam. The errors quoted are statistical (first) and systematic (second).

1.2.1 Decay Modes

Since charm quarks decay weakly into strange quarks, all of the decay modes in this study are modes that decay into Λ^0, Ξ_s^- and Ω_s^-. It is expected that the presence of a long-lived strange particle in the event may substantially reduce the large hadronic background. The following is a partial list of potential decay modes:

$$\Xi_c^+ \rightarrow \Lambda^0 K^- \pi^+ \pi^+ \quad (1.1)$$
$$\rightarrow \Xi_s^- \pi^+ \pi^+ \quad (1.2)$$
$$\rightarrow \Omega_s^- K^+ \pi^+ \quad (1.3)$$

$$\Xi_c^0 \rightarrow \Xi_s^- \pi^+ \quad (1.4)$$
$$\rightarrow \Xi_s^- \pi^- \pi^+ \pi^+ \quad (1.5)$$
$$\rightarrow \Lambda^0 K^- \pi^+ \quad (1.6)$$
$$\rightarrow \Omega_s^- K^+ \quad (1.7)$$

$$\Omega_c^0 \rightarrow K^- \Xi_s^- \pi^+ \pi^+ \quad (1.8)$$

This study is primarily focused in obtaining the cross sections of the decays $\Xi_c^+ \rightarrow \Xi_s^- \pi^+ \pi^+$, and $\Xi_c^0 \rightarrow \Xi_s^- \pi^+$. A search for the decay $\Xi_c^+ \rightarrow \Lambda^0 K^- \pi^+ \pi^+$ is also presented. The decay diagrams for these decays are shown in Figure 1.3.

Due to the extremely low lifetime of these states, it is somewhat difficult to extract them from the data. The typical decay distance in the lab frame is about 1.5 cm and 0.3 cm for Ξ_c^+ and Ξ_c^0 respectively, making the task of separating the primary and secondary interaction vertex somewhat difficult.

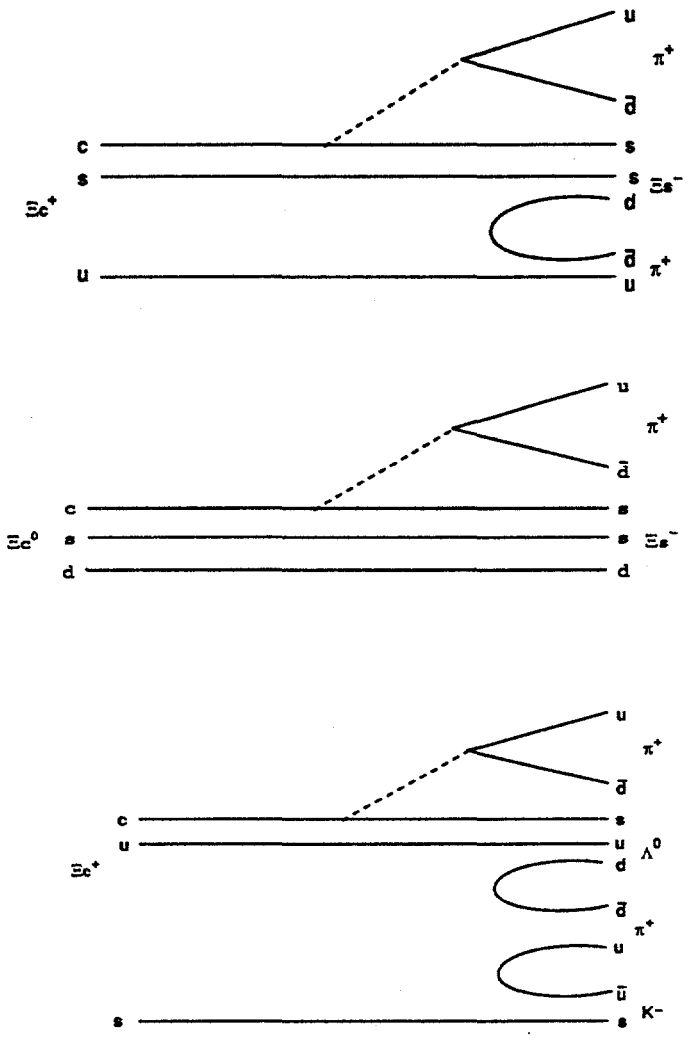

Figure 1.3: Some weak decays of charm baryons.

Chapter 2
The Detector

The analysis presented here was performed on data taken in the Tagged Photon Laboratory at the Fermilab Tevatron. The experiment, called E769, ran in the fixed-target period 1987-88. In its proposal, E769 stated,

> *We propose to measure the properties of hadronic charm production using the Tagged Photon Spectrometer facility. We shall measure the flavor dependence, x and A dependence of this process at the same time and in a single apparatus.*

In order to accomplish this goal, the experiment had to use a variety of beam particles and targets, together with the appropriate beam tagging devices, which were assembled for E769.

2.1 The Beam

The hadron beam used by the experiment was generated in the Tevatron. The Tevatron accelerates protons in five stages. The process starts with a negative hydrogen ion and a Cockcroft-Walton generator provides the first stage of acceleration at 750 KeV/c.

After leaving the Cockcroft-Walton, negative hydrogen ions enter a linear accelerator called the *Linac*. Once they are accelerated to 200 MeV/c, the hydrogen ions are stripped of their electrons and then they enter a synchrotron called the *Booster*. The Booster accelerates these protons to 8 GeV/c, then they enter into another

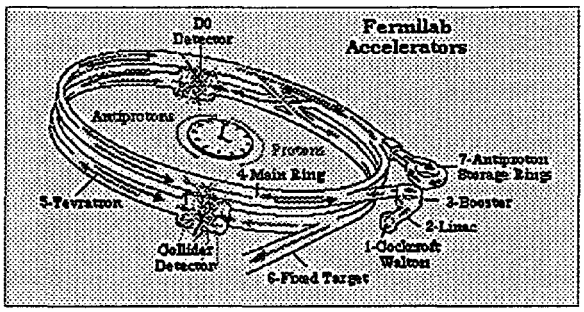

Figure 2.1: **The Tevatron:** The diagram shows the paths taken by protons and antiprotons in Fermilab's five accelerators. The beam of particles begin as negative hydrogen ions at the right in the (1) Cockcroft-Walton accelerator. They continue down the short, straight section, (2) the Linac. As the beam of negative hydrogen ions enters the third accelerator, (3) the circular Booster, both electrons are stripped off leaving a proton beam. The protons are injected into the upper ring, the (4) Main Ring and then down into the lower ring, (5) the Tevatron. In fixed target mode, the proton beam is extracted and sent down the (6) Fixed Target beam line to the experimental areas. This diagram is a reproduction of a diagram published in the WWW server at Fermi National Accelerator Laboratory.

synchrotron called the *main ring*. The Main Ring accelerates protons to 150 GeV/c. At this point, the protons are injected into the *Tevatron*, which uses the same tunnel as the Main Ring, but with superconducting magnets. In the Tevatron the protons are accelerated to 800 GeV/c.

In the fixed target mode, protons were extracted in spills of 22 seconds every minute and sent out to the experiments in the fixed target area. These primary protons were grouped in buckets of 2 ns duration with a separation of 19 ns between buckets. The TPL primary proton beam interacted with a 30 cm. beryllium target producing a secondary beam composed of pions, kaons and protons that were transported to the experimental area. A dipole magnet downstream of the target selected beam particles with momentum of 250 GeV/c. The beam rate was $\sim 0.5 \times 10^6$ particles/s in the negative run period and $\sim 2 \times 10^6$ in the positive.[13]

2.1.1 The Beam Tagging

Since the experiment had to deal with a diverse set of beams, it was necessary to introduce beam identification devices. A differential Čerenkov counter was used to identify kaons. In the negative run period there was no need to use another tagging device since there was a small amount of antiprotons[14, page 30] ~1.5%. However, in the positive run period, it was necessary to introduce a device capable of discerning pions from protons; the Transition Radiation Detector.

The DISC

When the speed of a charged particle in a dielectric medium exceeds the speed of light in that medium, atoms in the vicinity of the particle emit radiation at a characteristic angle θ_c. The angle is determined from the relation

$$\cos\theta_c = \frac{1}{\beta \mathrm{n}}, \tag{2.1}$$

where **n** is the index of refraction of the medium and β is the Lorentz parameter v/c.

A differential Čerenkov counter is a device that can measure the speed of a particle by accepting Čerenkov light in a small annular slit at some fixed angle θ off the axis of the counter. Since the DISC (Differential Isochronous Self-collimating Čerenkov Counter) used a gas radiator and the momentum of the beam was fixed, by adjusting the pressure of the gas it was possible to use the counter to provide a signal for the presence of a given mass particle.

The DISC was 5 meters long and 0.5 meter in diameter. Its geometry accepted Čerenkov light at $\theta_c = 24.5$ mrad. It was filled with Helium and operated at room temperature and a pressure adjusted so that it could tag kaons, ~135 psi. Special runs, called *pressure curves*, were periodically taken to monitor the DISC pressure.

A diagram of the DISC can be seen in Figure 2.2. The Čerenkov light was reflected backwards by a mirror M; it passed through two correction elements, a coma

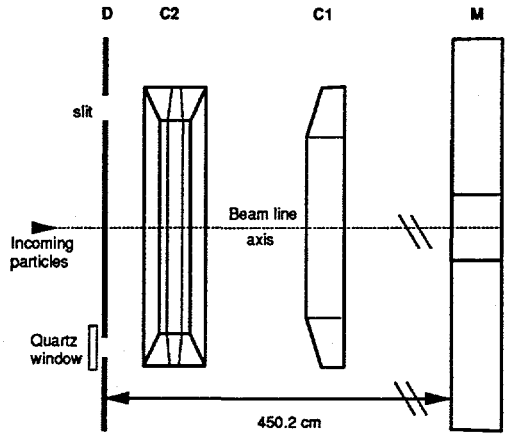

Figure 2.2: **The DISC**: D: diaphragm; C1, C2: Coma and chromatic corrector; M: Mirror.

corrector, C1, and a chromatic corrector, C2. The annular opening let Čerenkov light pass at a fixed angle only. The light was collected by eight PMT's evenly spaced around the annulus. Each PMT signal (2 per quadrant) was amplified and discriminated. Then these signals were wired into an electronic device so that whenever a 4-fold coincidence (at least 1 hit per quadrant) was detected a signal (**K-hi**) was sent to the trigger logic electronics, see Figure 3.1.[13]

The TRD

The main task of the TRD was to discern pions from protons. Transition radiation is produced whenever a charged particle, in uniform motion, passes suddenly from one medium to another. The particle induces a time dependent polarization in the medium and this polarization in turns emits radiation typically in a forward cone. The total energy of transition radiation[15] is given by

$$E = \frac{2}{3}\alpha\omega_p\gamma,$$

where γ is the known Lorentz boost factor, α the fine structure constant, and ω_p is the plasma frequency of the medium, given by

$$\omega_p = \frac{4\pi\alpha N_A\rho}{Am_e}$$

where N_A is the Avogadro's number, ρ the density of the medium, A the atomic mass and m_e the mass of the electron.

Since the total energy is directly proportional to γ, pions will emit more transition radiation than protons or kaons. Most of the radiation is produced in the X-ray domain and the mean number of X-ray photons emitted is proportional to α. It is therefore necessary to stack up several layers of thin material in order to collect enough energy. Destructive interference effects from the different layers must all be minimized.

The E769 TRD consisted of 24 identical modules. Each module, see Figure 2.3, included a total of 200-12.7μm polypropylene foils. Between the foils there were gaps of 180 μm that were filled with Helium gas. The passage of beam particles through the Helium-polypropylene boundary caused transition radiation. In order to detect the TR photons, a two-plane proportional wire chamber was adjoined downstream to each module. Each wire chamber consisted of 64 wires and was filled with a 90/10 mixture of xenon and methylal. Since gas xenon has a large cross section for X-ray photons, the PWC's can detect the ionized xenon gas. The gap between the PWC array and the radiator module was continuously flushed with nitrogen in order to avoid possible contamination of helium in the PWC planes. The threshold of each PWC array was set to pass photons with energies above 4 KeV.[16]

Since pions produced the most TR and protons emit the least, the particle tagging then was simply based on the number of PWC planes which fired. The output signal of each PWC plane was then sent out to a 48 bit coincidence register that was gated by two scintillator counters. The counters bracketed the TRD and their output was also used in the nearly-in-time coincidence detector, see Section 3.1.1 for more details. [1]

[1]This TRD paddle configuration was confirmed by Marleigh Sheaff.

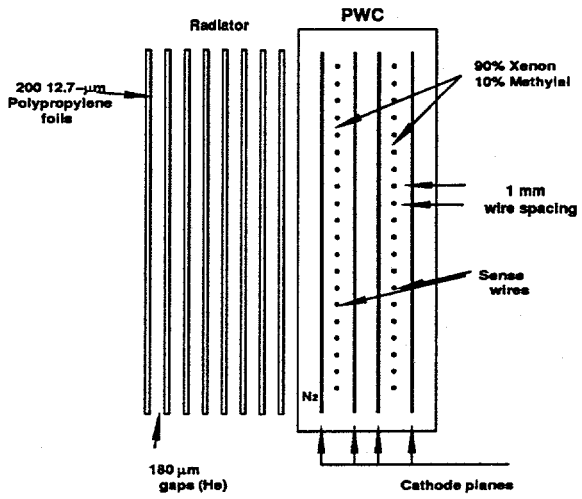

Figure 2.3: **The TRD**: Schematic of one E769 TRD module.

2.1.2 Beam Tracking and Beam Counters

In order to measure the beam trajectory, E769 included two types of track detectors. First, two arrays of 8 PWC planes were located approximately 31 meters upstream of the target. Each assembly consisted of 4 view planes (X, Y, X',W). Finally, a set of 2 silicon planes (X, Y) was located about 13 cm. upstream of the target. The intended task of this tracking array was to help to identify the location of the primary interaction vertex. The specification for these SMD planes can be seen in Table 2.4. Table 2.5 shows those for the PWC planes.

Upstream of the target and downstream of the two beam track silicon planes there were other two beam counters. The E769 trigger selection required a signal from the first counter (**Beam Spot** counter) and no signal from the second one (**Beam Halo** counter or **veto counter**) which had a hole cut in the middle, ensuring that a beam particle passed unobstructed towards the target. This pair of scintillators defined the **Good Beam** signal. See Figure 3.1.

Veto Counter Shield

It turned out that the two beam track silicon planes were very noisy, and it was not possible to use them to better locate the primary interaction vertex. It was

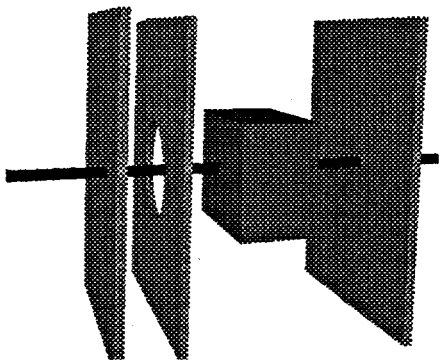

Figure 2.4: **The beam counter array**: From left to right, the beam spot, the beam halo, the target and the interaction counter.

later discovered by people of E791, the experiment that ran after E769 completion at TPL, that after removing the silicon planes the **veto counter** was noisy too, probably due to nuclear fragments from back-scattering in the first target foils. It was necessary then to look for any anomalies in the E769 beam-veto counter. Paul Karchin looked at the beam-spot ADC and it was felt that the two silicon planes provided an effective shield to that counter.

A last scintillator counter, known as the **Interaction** counter, was located downstream of the target. Its main purpose was to determine if the beam particle interacted in the target. The threshold of this counter was set to 5 minimum ionizing particles.

2.1.3 The Beam Composition

E769 recorded about 400 Million physics events with hadron beam composed of pions, protons and kaons. The incident numbers of beam particles are summarized by run period, in Table 2.1. See Table 2.2 for run period definitions. A more detailed description of the beam count elements can be found in reference [13].

	Region 2	Region 2	Region 3	Region 4
π^-	11.5	5.86		
K^-	0.5688	1.69		
π^+			105.	8.08
K^+			5.58	0.00887
p			54.6	2.83

Table 2.1: **E769 incident beam particles.** The counts are in billions (10^9) of events. This count does not include upstream beam losses.

REGION	Beam energy	Beam polarity	DISC	beam hadron type
1	210	negative	K	π and K
2	250	negative	K	π and K
3	250	positive	K	π, K and p
4	250	positive	p	π, K and p

Table 2.2: **E769 run regions.**

The following list shows the total number of physics triggers recorded.

- 150 M π^-.
- 25 M K^-.
- 87 M π^+.
- 70 M K^+.
- 70 M protons.

E769 Run Regions

Due to the variety of E769 target and beam types, some definitions are needed in order to distinguish the different run conditions. Table 2.2 shows these definitions.[2]

[2]Entries in the DISC column show which type of beam hadron the DISC was calibrated for.

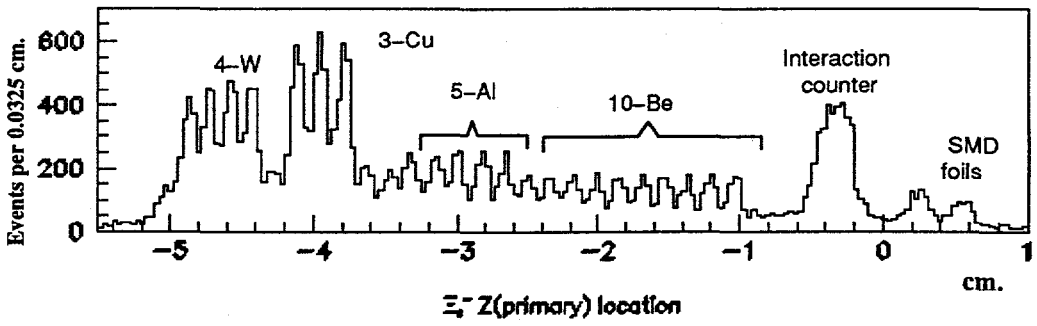

Figure 2.5: **Target:** Identified primary interaction location of Ξ_s^-. The vertical scale represents number of events and the horizontal is the **Z** position of the vertex. Between the copper and the aluminum foils there are 2 beryllium foils, there is one hidden beryllium foil upstream of the first tungsten foil and one between the tungsten and the copper foils.

2.2 The Target

Since one of the goals of E769 was to measure the atomic mass dependence of the charm cross section, it was necessary to include several target materials. Four different materials were used: tungsten, copper, aluminum and beryllium, and they were distributed among 26 thin foils. Annular paper washers separated the foils by 1.36 mm. The whole target assembly was encased in a plexiglas box. Figure 2.5 shows the identified primary interaction vertex of Ξ_s^- decay candidates. Table 2.3 presents the complete specification of the segmented target.[3]

2.3 The Spectrometer

The TPL Spectrometer (TPS) is a typical general purpose detector. It consists of several specialized single task detectors integrated in one big device. TPS has tracking capabilities provided by Silicon Microstrip detectors, Drift Chamber detectors, and 2 Proportional Wire chamber planes. It can also measure the momentum and

[3]This is a reproduction of similar table in [13] page 56.

Foil #	Material	Thickness $\pm \sim 0.006$ (mm)	Interaction Lengths % ($\pm \sim 3\%$)	Radiation Lengths % ($\pm \sim 3\%$)	Z-position of foil (mm) ($\pm$0.005mm)
1	Be	0.250	0.0614	0.0708	43.468
2	W	0.097	0.101	2.8	41.832
3	W	0.095	0.0991	2.7	40.393
4	W	0.094	0.0980	2.7	38.928
5	W	0.097	0.101	2.8	37.458
6	Be	0.255	0.0627	0.0722	35.999
7	Cu	0.250	0.166	1.75	34.376
8	Cu	0.258	0.171	1.80	32.758
9	Cu	0.253	0.168	1.77	31.130
10	Be	0.276	0.0678	0.0782	29.494
11	Be	0.244	0.0600	0.0691	27.857
12	Al	0.249	0.0632	0.28	26.248
13	Al	0.257	0.0652	0.29	24.625
14	Al	0.251	0.0637	0.28	23.013
15	Al	0.251	0.0637	0.28	21.394
16	Al	0.253	0.0642	0.28	19.770
17	Be	0.266	0.0654	0.0754	18.143
18	Be	0.256	0.0629	0.0725	16.522
19	Be	0.267	0.0656	0.0756	14.899
20	Be	0.266	0.0654	0.0754	13.259
21	Be	0.263	0.0646	0.0745	11.634
22	Be	0.261	0.0641	0.0739	10.036
23	Be	0.262	0.0644	0.0742	8.386
24	Be	0.245	0.0602	0.0694	6.770
25	Be	0.263	0.0646	0.0745	5.155
26	Be	0.255	0.0627	0.0722	3.527

Table 2.3: **Target Specifications:** Z-position of foil is measured from the upstream side of the foil to the target reference surface which is the downstream end of the target container.

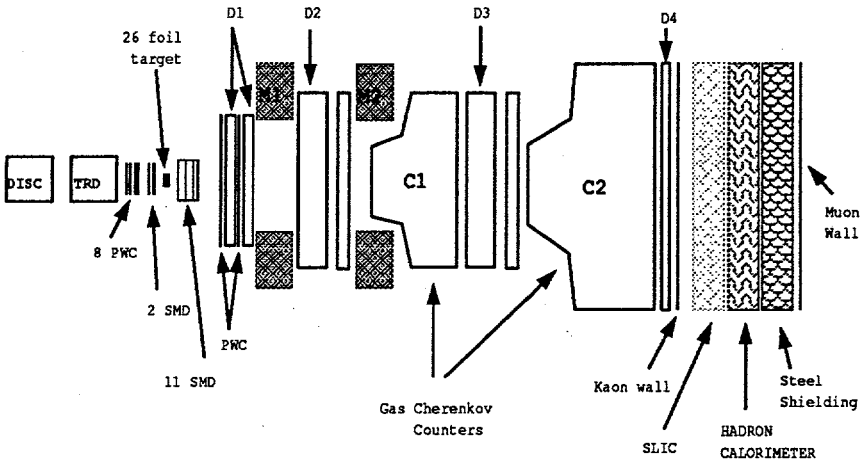

Figure 2.6: **The Tagged Photon Spectrometer**: DISC, TRD: beam identification devices; 8-PWC, 2-SMD: beam tracking detector; Target; 11-SMD, D1, D2, D3, D4: charged particle tracking detector; M1, M2: analyzing magnets; C1, C2: charged particle identification; Kaon wall; SLIC: electromagnetic calorimeter; Hadron calorimeter; Muon wall.

charge of non-neutral particles with two large-aperture magnets. The particle identification capabilities are provided by two Čerenkov counters, and muon wall. It also has electromagnetic and hadronic calorimeters that provided the main trigger of the detector. The Spectrometer is shown schematically in Figure 2.6

2.3.1 Tracking

One of the strengths of fixed target experiments is the ability to reconstruct the trajectory of charged particles with high precision. The E769 spectrometer tracking devices included 11 Silicon Microstrip Detector planes (SMD), 35 Drift Chamber planes grouped in 4 stations D1-D4, 2 PWC planes, and two magnets for momentum determination.

The Vertex Detector

Fixed target spectrometers have benefited greatly by introducing high resolution vertex detectors. A vertex detector is a device capable of resolving the daughter particles of the charm decay from those of the primary vertex interaction. E769

used solid state detectors known as Silicon Microstrip Detectors.

Silicon Microstrip Detectors

The E769 Silicon Microstrip Detectors are based on the p-n junction diode. These diodes came as high resistivity silicon crystals doped with a layer of arsenic in one side and micro-strips of boron in the other, see Figure 2.7. In a crystalline structure with many atoms, the atomic levels of each atom combine to form bands of allowed energy states and gaps between these bands. The gap between allowed zones is typically 5-10 eV. The last band filled with electrons is called the valence band, and the next higher energy band is called the conduction band. In a good conductor the valence band is not very populated. However, in an insulator the valence band is completely filled, so that very high temperature is needed in order for electrons to reach the conduction band and move freely. In a semiconductor on the other hand, like silicon, the valence band is completely filled but the energy gap is shorter, $\sim$1 eV. Therefore a few electrons can reach the conduction band and move freely in the crystal. Silicon has 4 valence electrons, and when a silicon crystal is doped with arsenic, which has 5 valence electrons, then arsenic atoms may replace some silicon atoms, introducing an extra free (conduction) electron in the crystalline structure. This is an n-type semiconductor since a negative charged electron is introduced. Boron, on the other, hand has 3 valence electrons. Therefore, when silicon is doped with boron, the crystalline structure lacks one electron. This is a p-type semiconductor since the missing electron or hole behaves as one positive free charge in the crystal.

When p-type and n-type semiconductors are joined, to make a p-n junction diode, free electrons in the n-type portion diffuse and fill the holes of the p-type portion establishing a potential difference across the boundary. This region in the boundary is devoid of moving charges and it is called the depletion region. It can be enhanced by supplying more electrons to the n-type end of the diode with a power supply (reverse bias regime). The n-type region is then essentially emptied of electrons and

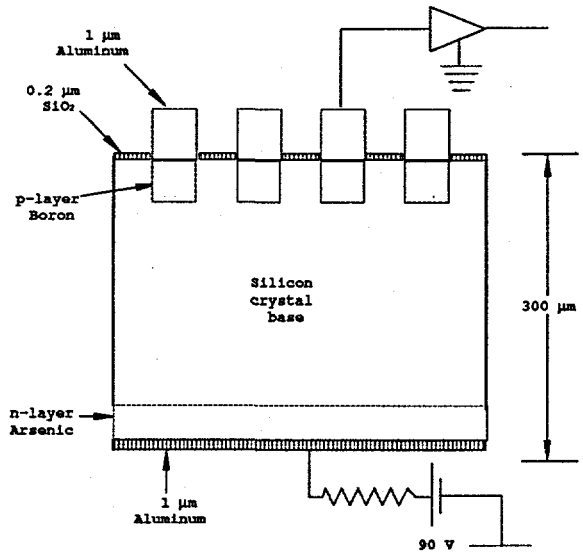

Figure 2.7: Cross section of the Silicon Microstrip detector.

the p-type of holes or the valence band is completely filled, and the only way to produce a current across the junction is by ionization. Typically atoms in the diode need only 3.6 eV to be ionized[17, 18].

The E769 SMD

E769 used 9 planes introduced by E691 and introduced 4 more planes of its own. Two of these were placed upstream of the **beam counter**, Station 4 in Table 2.4, and they have already been described in Section 2.1.2. The other two, Station 5 in Table 2.4, were placed downstream of the **Interaction Counter**. A detailed specification of these planes can be seen in Table 2.4.

The Drift Chambers and PWC's

Whenever a charged particle passes through a gas medium it can leave a trail of ionized gas and electrons. Both drift chambers and proportional wire chambers are detectors that can collect this ionized gas and electrons and provide an electrical signal indicating the passage of the particle.

In both types of chambers the electrons are collected in a wire (the anode) which is kept at some high voltage. Electrons and ions then can be accelerated in the

Station Number	Box	Views	Pitch μm	Instrumented Channels	Nominal Z cm
4	1	X	25	386	-17.044
			50	0	
		Y	25	386	-17.263
			50	0	
5	2	X	25	386	0.605
			50	304	
		Y	25	386	0.202
			50	304	
1	3	X	50	512	1.931
		Y	50	512	2.934
	4	V	50	512	6.658
2	5	Y	50	768	10.977
		X	50	768	11.328
	6	V	50	768	14.937
3	7	X	50	1000	19.853
		Y	50	1000	20.202
	8	V	50	1000	23.825

Table 2.4: The SMD array.

electric field and produce secondary ionization close to the anode wire resulting in an amplified signal.

The difference in the two types of chambers originates is that a PWC uses the closest wire hit to measure the location of the passing particle while a drift chamber attempts to measure the drift time of ionization electrons in the gas and by knowing the drift speed it is possible to get more precise measurement of location of the passing particle. Drift chambers also include an extra wire per each sense wire, the field shape wire, that serves to establish a constant electric field over the drift region.

Tables 2.5 and 2.6 show the specifications for the PWC and drift chambers. The chambers were grouped in 4 stations, D1 through D4. D1 had two assemblies of 4 planes each, 8 planes total. Each assembly could obtain the (x,y) coordinates of a track. Since these two assemblies did not directly measure the Y coordinate, upstream of each of the two assemblies a **Y** PWC plane was introduced. D1 was located upstream of the first magnet. Between the magnets, there was D2, with 4 assemblies of UXV planes, 12 planes total. Then downstream of the second magnet, there was D3 with another 4 UXV planes. Finally, D4, with one UXV assembly downstream of the second Čerenkov counter.

The Magnets

TPS has two large-aperture magnets, **M1** and **M2** in Figure 2.6. They were roughly about the same size but since M2 was farther downstream, its angular acceptance was lower.

The task of the magnets is to determine the momentum and electrical charge of charged particles. This is basically done by measuring the entrance and exit trajectories (tracks) of the charged particle in the magnet. The magnetic field is aligned perpendicular to the beam line and parallel to the vertical axis making the vertical component of the trajectory of the particle almost unaffected by the magnet, which allows one to match an entry-exit pair. A fit is done to the composed

Station	Assembly	Views	Wire spacing cm	Sense Wires	Nominal Z cm
BEAM1	1	X	0.1	64	-3157.0
	2	Y	0.1	64	-3156.0
	3	X'	0.1	64	-3155.0
	4	W	0.1	64	-3153.0
BEAM2	5	X	0.1	64	-1226.0
	6	Y	0.1	64	-1224.0
	7	X'	0.1	64	-1223.0
	8	W	0.1	64	-1222.0
P1	1	Y	0.2	288	130.10
P1	2	Y	0.2	288	175.40

Table 2.5: **The PWC detectors**: PWC specifications. The planes X and X' in BEAM1 & BEAM2 are offset by 1/2 the wire spacing. The W planes are at 30° to the horizontal (X). All of the stations used a mixture of 83% Argon 17% CO_2 0.3% Freon.

entry-exit track in order to get trajectory and charge parameters.[4]

The magnetic field of both magnets was accurately mapped at TPS in experiment E516. E769 used these measurements and introduced an overall calibration factor to make sure that the mass of the K_s meson was correct within 0.1 MeV of the known value. Table 2.7 shows some characteristics of the magnets.

2.3.2 Particle Identification

The Threshold Čerenkov Counters

Charm particles decay predominately into final states containing strange mesons and hyperons, which decay into protons and pions. The TPS has two Čerenkov counters, C1 and C2 in Figure 2.6, to help discriminate kaons and protons from the more copiously produced pions.

The light radiated satisfies Equation 2.1, and for charged particles between 6 and

[4]All of this is done in offline reconstruction software.

Station	Assembly	Views	Cell size cm	Sense Wires	Nominal Z cm
DC1	1	U	0.4763	192	153.6141
		V	0.4763	192	154.5666
		X	0.4761	192	158.6941
		X'	0.4761	96	159.6466
	2	U	0.4763	256	188.7144
		V	0.4763	256	189.6669
		X	0.4761	256	193.7918
		X'	0.4761	96	194.7443
DC2	1	U	0.8922	176	382.3691
		X	0.9525	192	383.9566
		V	0.8922	176	385.5441
	2	U	0.8922	176	424.9090
		X	0.9525	192	426.4965
		V	0.8922	176	428.0840
	3	U	0.8922	208	466.6463
		X	0.9525	224	468.2338
		V	0.8922	208	469.8213
	4	U	0.8922	208	497.7105
		X	0.9525	240	499.3081
		V	0.8922	208	500.9058
DC3	1	U	1.4870	160	928.2963
		X	1.5875	160	929.8838
		V	1.4870	160	931.4173
	2	U	1.4870	160	970.8413
		X	1.5875	160	972.4288
		V	1.4870	160	974.0163
	3	U	1.4870	160	1012.5862
		X	1.5875	160	1014.1737
		V	1.4870	160	1015.7612
	4	U	1.4879	160	1044.3693
		X	1.5875	192	1045.9669
		V	1.4870	160	1047.5646
DC4	1	U	2.974	128	1737.8959
		X	3.175	160	1743.5855
		V	2.974	128	1749.2751

Table 2.6: **The Downstream track detector**: Drift chamber specifications. The planes X and X' in D1 are offset by 1/2 the wire spacing. U and V planes are at $\pm 20.5°$ of the vertical(Y). All of the stations used a 50%-50% mixture of Ar-ethane and a small admixture of ethanol for quenching and age prevention.

	Current Amperes	$\int Bdl$ T-m	p_t kick MeV	Z(center) cm
M1	2500	0.71	213	286.6
M2	1800	1.07	321	620.6

Table 2.7: Magnet data

60 GeV, and a refraction index close to 1, the Čerenkov angle is ~10-20 mrad. The Čerenkov counter design is remarkably simple; a gas chamber filled with Nitrogen in C1 and 80-20% Helium-Nitrogen mixture in C2, operating at normal pressure and temperature and a segmented mirror arrangement to collect the light.

The photon yield is momentum dependent, in fact Equation 2.1 shows this since $\cos\theta_c \leq 1$ and therefore

$$|\vec{P}| \geq \frac{mc}{\sqrt{n^2-1}}.$$

The formal photon yield relationship [5] is written in the equation below, see [19, page 638] or [15, 20]

$$\frac{dN}{dx} = 2\pi\alpha \int (1 - \frac{1}{\beta^2 n(\lambda)^2})\frac{d\lambda}{\lambda^2}.$$

where

$$\begin{aligned} dN/dx &= \text{photon yield per unit length,} \\ \alpha &= \text{the electromagnetic coupling constant,} \\ \beta &= v/c \text{ Lorentz parameter,} \\ \lambda &= \text{wavelength,} \\ n(\lambda) &= \text{the medium's index of refraction.} \end{aligned}$$

Figure 2.8 is a graphical representation of the photon yield as a function of momentum and it clearly shows the thresholds for different particles. A particle can be identified above its threshold just by counting the number of photons emitted.

[5] When dealing with real detectors, this relationship must also include an *ad. hoc.* λ dependent weighting function that represents the detector efficiency.

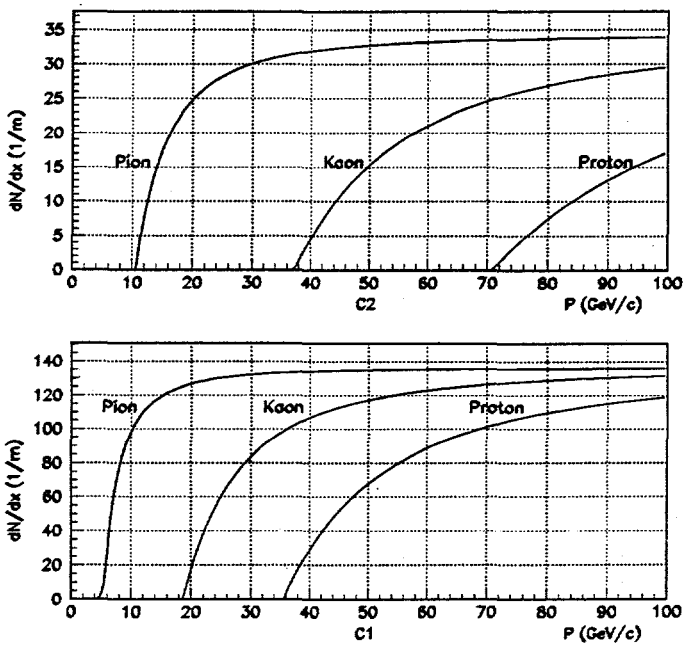

Figure 2.8: Response of the Čerenkov counters. The efficiency has been set to 1.0 between 1600$\AA$ and 5000$\AA$ and zero all other ranges and the refraction index n has been assumed to be constant.

The segmented mirror arrangement was designed to minimize the number of times particles would share the same segment. The reflected light of each of the segments was collected by a set of Winston-cone photo-multipliers (one PMT per segment). The light in C2 was reflected by a secondary mirror before being collected by the photo-multipliers, see reference [20, pages 59 and 61].

The Muon Wall

The last device in TPS was a muon wall. Most hadrons were stopped by a steel wall. The steel, located downstream of the hadrometer, is made from five layers of 8-inch thick rolled ingots — all welded together.[6] Upstream of this wall there was an array of plastic scintillators that detected particles that passed the steel wall only, mostly muons.

[6]Information provided by Jeff Appel by private communication

2.3.3 Calorimetry

TPS had two calorimeters for the detection of hadronic and electromagnetic showers. All detectors of the TPS described so far try to measure quantities like momentum, trajectory and so forth. This implies disturbing as little as possible the state of the particle. Calorimeters, on the other hand try to completely destroy the original state of the particle by forcing it to yield all of its energy.

The calorimeters were used exclusively to trigger the detector.

The Electromagnetic Calorimeter

The electromagnetic calorimeter was based on segments of and scintillation material. The segmentation provided a way to measure the position of the electromagnetic shower. The calorimeter was broken in 60 layers of scintillator-absorber pair, with the absorber portion made of metal sheets composed of Al-Pb-Al. The radiator container design included a square-wave-corrugated aluminum sheet. The corrugations provided a channel where scintillator liquid was contained and they came in three different alignments, so they provided UVY views of the shower. UV views were shifted $\pm 20.5^0$ from the vertical Y view. The scintillation medium was a mineral oil liquid, NE235A. This device is called the SLIC or Segmented Liquid Ionization Calorimeter.

The Hadronic Calorimeter

Just downstream of the SLIC was the hadronic calorimeter. The absorber of the calorimeter consisted of 18 2.54 cm thick steel plates alternating with plastic scintillator. The scintillators were strips 14.48 cm. wide which were arranged to measure X and Y positions of the hadronic shower.

Chapter 3
The Data

E769 wrote to magnetic tapes about 400 Million physics events. The descriptions of the triggering system and the Data Acquisition system are summarized in this chapter.

3.1 The Trigger

To accomplish its main goal E769 planned seven triggers, but only five of them were actually carried out. A simplified view of the trigger, as well as the logic diagram and some important scalers can be seen in Figure 3.1. The final judgment as to whether an event would be triggered was executed by a programmable logic unit (PLU). A simplified view of the E769 triggers can be seen in Figure 3.2. These triggers were: Interaction, E_t(pi), E_t(kaon), E_t(beauty), and Electron. [21]-[23].

3.1.1 The Killer Bit

The experiment was set up so that the DISC would be the kaon tagging device. When no kaon was detected, the TRD would tag pions and protons. The TRD had a long time-window for the tagging operation, and it could become confused when another beam particle arrived within this window. In order for the TRD to do the tagging unambiguously, it required that there be no additional beam particles within ~150 ns of the beam particle. A *"nearly-in-time beam particle detector"* circuit was implemented; if no "nearly-in-time beam particle" was detected, a TRD SAFE or a *killer bit off* signal was sent to the PLU. A similar device was not necessary for the

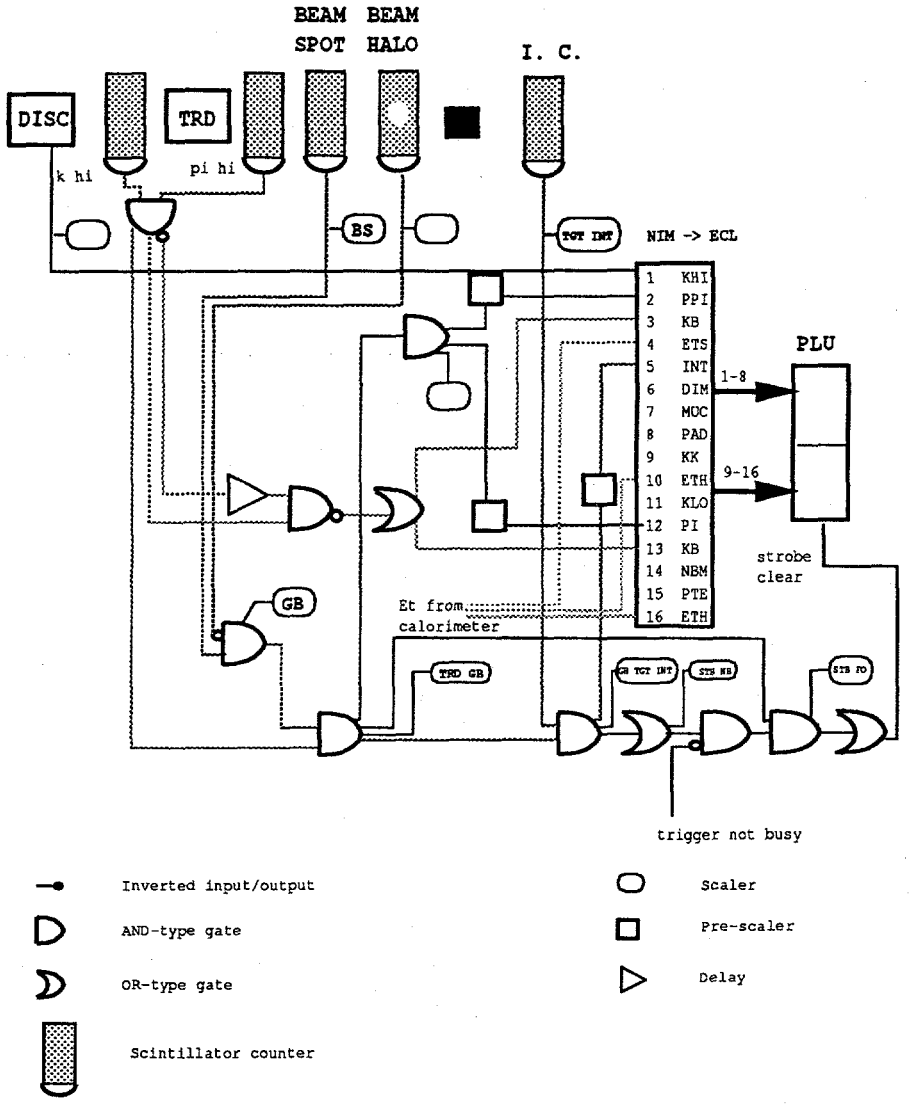

Figure 3.1: Logic Diagram. Simplified view of the E769 trigger and logic diagram.

DISC since its time window was fairly narrow. [1]

3.1.2 Interaction

At the lowest level there was the so-called Interaction trigger. As explained in Section 2.1.2, the coincidence between the **Beam Spot** counter in anti-coincidence with the **Beam Halo** counter defined the **Good Beam** signal. Downstream of the target another counter (**Interaction** counter) would fire whenever a hadron-beam caused an interaction; this was done by setting a threshold on the output of the counter requiring a signal equivalent to five or more minimum ionizing particles. This signal defined a **Target Interaction**. **Good Beam** and **Target Interaction** signals were combined in an AND-type gate that defined the Interaction Trigger.

While the experiment was running in negative-beam mode, the beam was composed of 93% pions. Later when the experiment switched to positive-data run, it was necessary to distinguish between pions and protons. This task was done by the TRD and, as explained in Section 2.1.1, the device was gated by a pair of scintillator counters. These TRD-scintillator counters also provided an output signal to the trigger logic. This signal called **TRD** was combined with **Good Beam** signal in an AND-type gate to form the **TRD Good Beam** signal for the Interaction trigger.

Prescalers

As it was mentioned in Section 2.2, the approximate size of the target was about $\sim$2% of an interaction length; this means that roughly $\sim$2% of the time an interaction will occur. Since the beam rate was 1 MHz, it would imply about 20 thousand interactions every second, a rate too high for the Data Acquisition System. This rate was then lowered by the placement of prescaler devices. The Interaction trigger was prescaled by a factor of 100 to 500.

---

[1] The killer bit was implemented while running in the positive beam period when beam rate was very high.

E_t triggers

All other triggers in E769 were based on the transverse energy of the event as measured in the electromagnetic and hadronic calorimeters. The reason for triggering the detector on the transverse energy is that events containing charm particles have a higher transverse momentum than minimum bias events containing only lighter quarks. The transverse energy in the calorimeter is measured by weighting the signals from the SLIC and the hadrometer proportionally to the distance away from the beam line. Two thresholds were used: E_t(standard), the lowest, required an energy between 5 and 6 GeV, depending on the run. The higher threshold, E_t(high), required a threshold of 8 GeV.

E_t(kaon)

This trigger required an E_t(standard) and a kaon-beam signal from the DISC. This trigger was not prescaled since kaon beam represented only 6% of the beam composition.

E_t(pi)

The trigger E_t(pi), required **TRD-GOOD BEAM** signal, E_t(standard), and also the Killer bit off. This trigger was also prescaled.

Electron

This trigger was installed in the positive data run to enhance the detection of semileptonic decays of B mesons. It required the high E_t setting as well as a large deposition of energy in the SLIC consistent with an electron signal. It was not prescaled.

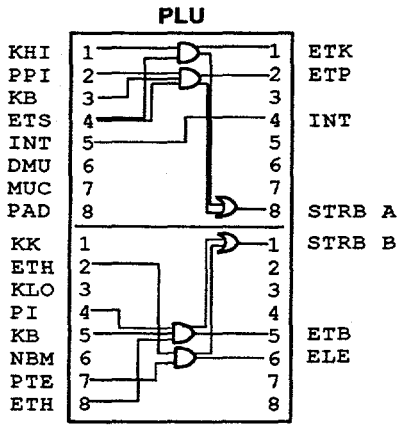

Figure 3.2: **PLU:** Programming of the PLU.

E_t(beauty) or E_t(high)

This trigger required E_t(high) setting from the calorimeters, a TRD-id signal, which was prescaled but to a different rate from that of E_t(pi), and also required the killer bit off.

3.2 The Data Acquisition System

E769 introduced a new Data Acquisition System to TPL. The objective was to achieve an output rate of ~400 events/s with only 30% dead time. A relative high output rate was necessary because the hadronic cross section for charm is small relative to the total cross section. The high rate then is a way to accumulate many events.

The DA system was based in a parallel architecture. As described earlier TPS is a very complex detector. It is in fact a sort of segmented detector that includes 3 types of tracking detectors, 2 calorimeter detectors, beam tagging devices, and so forth. The output of each of these segments, must be digitized, built as an integrated event, and stored.

Once an event had passed the trigger selection criteria, it was stored in seven special electronic devices called Smart Crate Controllers (SCC). Each of the SCC

modules contained then a fragment of an event and they were resident in the Camac module.

The SCC modules were based on a Motorola 68000 processor, that worked in conjunction with the Camac controllers. Each SCC module was programmed so that it could read the resident fraction of event and send it to a dedicated read-out buffer module, called RBUF.

Each VME-resident RBUF was double buffered allowing a processor to read one while the SCC was filling the other.

The read-out, compression and formatting of each fragment of event in RBUF was done by processor modules built at Fermilab. E769 used 17 ACP (Advanced Computing Project) modules. The ACP modules were able to work in parallel, processing a fragment of an event. They perform 3 different tasks. First, there was one that coordinated the operations of all the others, the BOSS ACP. The 16 remaining modules, *event handlers*, were dedicated to read out the event fragments from RBUF, compress and format the entire event. At any given moment during a spill, two of the event handlers performed the read-out from RBUF *grabbers*. Then the other 14 performed the data compression and formatting, *munchers*.

The task of which event handlers would be *munchers* or *grabbers* was carried out by the BOSS ACP. The boss ACP also performed the task of deciding which events went to tape and to a VAX11/780.

The highest level of control of the DA was executed by the VAX system, and the operators in charge. It allowed an operator to start, stop, pause, resume and abort runs. It also allowed for the monitoring of the whole system while running.

3.3 Reconstruction

E769 recorded about 400 million events on 10000 6250 bpi magnetic tapes. The reconstruction of the data was carried out in several stages. The first stage, called

PASS0, was a run through the first few thousands of events. It calculated pedestals and conversion factors from ADC counts to energies. It also generated several useful distributions, like TRD plane counts, plane efficiencies and so on.

The second stage, called PASS1, performed the tracking reconstruction. PASS2, the third stage, performed Čerenkov and calorimetry analysis. PASS2 also performed the vertex fitting, that is, it generated a list of secondary vertices and a primary vertex. PASS2 compressed the input data into Data Summary Tape format, DST.[2]

3.3.1 The Pair Strip Filter

At DST level, the 370 million events were compressed in ~500 8mm tapes. This number of tapes is too large a number to handle, and therefore a filter must be applied in order to reduce the amount of data to analyze. The filter called *pair strip* included a set of cuts to enhance the presence of charm mesons.

Since charm mesons decay hadronically mostly into 2 or 3 charged particles, the idea was to impose cuts on a track pair that might potentially come from charm meson decay.

If the pair actually came from a charm meson decay, it was necessary to check that they were not part of the primary interaction vertex. If any track of the pair is part of the primary vertex, then the primary vertex must be re-fitted without these tracks.

The list in page 36 summarizes the cuts used every time a pair is tested. The primary vertex re-fit is not in this list but it was done once per event. Also, events must have at least 2 tracks with JCATSG ≥ 3 or JCATSG ≤ 15.

---

[2]Part of the data was reconstructed to PASS2 and a DST format later.

About JCATSG

As it was described in Chapter 2, the spectrometer is ordinarily divided in four different geometrical regions. The DST output format contains a word for each reconstructed track, named JCATSG, that contains information[26] specifying in which sets of Drift Chamber planes the track is detected. Consequently, the n-th bit of this word is set if the track is detected in the n-th Drift Chamber detector, a fifth bit may be set if the track shares too many hits with other tracks.

Pair Strip Filter Cuts

A short description of the cuts used in the pair strip is presented below. For a schematic representation of the cuts please refer to Figure 4.1.

σ_z(vertex)

Error in the Z coordinate determined from a constrained fit of tracks to a common vertex.

Z(vertex)

Z coordinate of the vertex. It must not lie upstream of the edge of the target.

χ^2/n of Secondary Vertex

The reduced χ^2 of vertex from the fit, it is obtained by doing a constrained fit of tracks to a common vertex.

SDZ

This quantity measures the separation of the secondary from the primary vertex. It is calculated as:

$$\mathrm{SDZ} = \frac{Z(\textsc{secondary}) - Z(\textsc{primary})}{\sqrt{\sigma_z^2(\textsc{primary}) + \sigma_z^2(\textsc{secondary})}}$$

RAT

A random combination of two tracks may form an optimum vertex very frequently. If the pair was produced by a decay from the primary interaction vertex, those two tracks probably do not point back to the primary vertex at all. The RAT cut was introduced to do just that, and is defined as

$$\mathrm{RAT} = \prod_{i=1}^{2} \frac{d_i^s}{d_i^p}$$

where d_i^s and d_i^p measure the impact parameter of each track of the pair to the secondary and primary vertex respectively.

PT2DK

The scalar sum of the transverse momentum components to the parent direction of the decay products.

1. Event must have a primary interaction vertex
2. Z(re-fitted primary) ≥ -6.0 cm.
3. Z(secondary vertex) ≥ -6.0 cm.
4. σ_z(secondary vertex) ≤ 0.180 cm.
5. χ^2/n(secondary vertex) ≤ 5.0
6. SDZ ≥ 6.0
7. RAT ≤ 0.06
8. PT2DK $> 0.1(\mathrm{GeV})^2$.

Chapter 4
Signal Extraction

This section details the selection criteria for Λ^0, Ξ_s^-, Ω_s^-, Ξ_c^+ and Ξ_c^0 decays. All of these signals were extracted from all 43 pair-strip tapes, which represent about 40 Million events.

Whenever a signal is to be extracted from a data sample, a set of cuts has to be applied so that the significance of the signal is maximized. A subset of these cuts is fixed, in the sense that the physics of the given decay mode demands the cut to be satisfied in rigorous way, e. g. the tracks that make a Λ^0 candidate have to have opposite charge. Other cuts, however, have to be adjusted to some *appropriate* value, e.g., how closely may the decaying particle approach the primary interaction location.

The appropriate value for this last type of cut cannot be chosen arbitrarily, it must be set accordingly with the underlying physics and in a way that statistical fluctuations are not enhanced by the value of the cut. The next section deals with the study of cuts and the significance of signals.

4.1 Statistical Significance and Cut Adjustment

In order to find the appropriate value of an adjustable cut the significance of the signal is maximized. Significance being defined as

$$\mathrm{S} = \frac{\mathrm{Signal}}{\sqrt{\mathrm{Signal} + \mathrm{Background}}},$$

where Signal and Background refer to the number of events found in the Signal peak

and under it respectively. In this way, and interpreting the outcome using Gaussian statistics, a signal with significance of one is said to have a probability of 68% of being a true signal and 32% probability of being statistical fluctuation.

One way of doing this study is to get a set of histograms for different values of the variable to cut, and from the fits of the histograms to obtain the significance. Although precise, this method is very time consuming and tedious. Another approach is to assume a flat (zero-slope) background combined with a Gaussian signal; since fractions of signals and backgrounds are known, it is possible to get the distributions of signal and background as functions of the variable to cut. There are several problems with this method; the first is the assumption of a flat background that is not always met, for various reasons such as cuts too loose, shape of phase space, and location of signal in it. Another difficulty is that the method can be applied to stable particles but not to resonant states. This problem can be avoided with a few modifications. The last problem, and probably the most difficult, is the fact that *some amount of signal needs to be present* in order to get signal and background distributions. Normally this is not a problem when signals greater than 50 or 100 events are expected, but for low statistics searches the method has to be modified since even if a signal is pulled out of the data, there is a greater risk in enhancing a statistical fluctuation.

The cuts for high statistics decays like Ξ_s^- and Λ^0 were adjusted using this technique. The technique is being setup and described in detail in a Fortran library by David Passmore. For an example see Appendix A.

In order to avoid enhancing a statistical fluctuation, the significance of the signal must be calculated so that the signal is taken from the Monte Carlo simulation and the background from the real data events. Since it is always extremely easy to get a reliable signal from the Monte Carlo simulation, one avoids the problem of requiring harsh cuts in order to get a signal. [1] The method starts by obtaining a histogram,

[1]This is due to the fact that the signal *is* in the simulated data and there is minimal background.

H1, of the variable that is intended for study, within 2.5σ of the central value of the mass of the decaying particle. This histogram then contains the total Monte Carlo signal and some amount of background. In order to subtract this amount of background, a second histogram, H2, for the variable is made so that events outside the 2.5σ region or sidebands are taken.[2] Now a background subtracted histogram, H3, is made so that, H3 = H1 - f*H2, the factor f may be easily calculated by assuming a flat background, a condition that is usually met by Monte Carlo data. Finally, a histogram of background from the real data is made, just like H3, and now the significance can be obtained provided that the signal from the Monte Carlo simulation, H3, is normalized to the expected number of real data events.

4.2 Cuts

A short description of the cuts used to get the signals is presented below and some of the cuts are shown schematically in Figure 4.1.

SPD

Shortest Perpendicular Distance between two tracks. This is a geometrical calculation based on the condition that a line intersecting both tracks would be perpendicular to them. As a complementary result it also is possible to get the coordinates of the intersecting point, therefore the actual routine that does the work is in fact a basic vertex fitter. This cut is necessary since it's the only way of getting a vertex when using DC tracks,[3] as in a Λ^0 search or when is necessary that a decay candidate be promoted to a track and all error matrix information is lost.

---

[2] In order not to extract any signal the sideband is started at 3.5σ away from the central value.

[3] No error matrix information for DC tracks was recorded on most of the DST tapes.

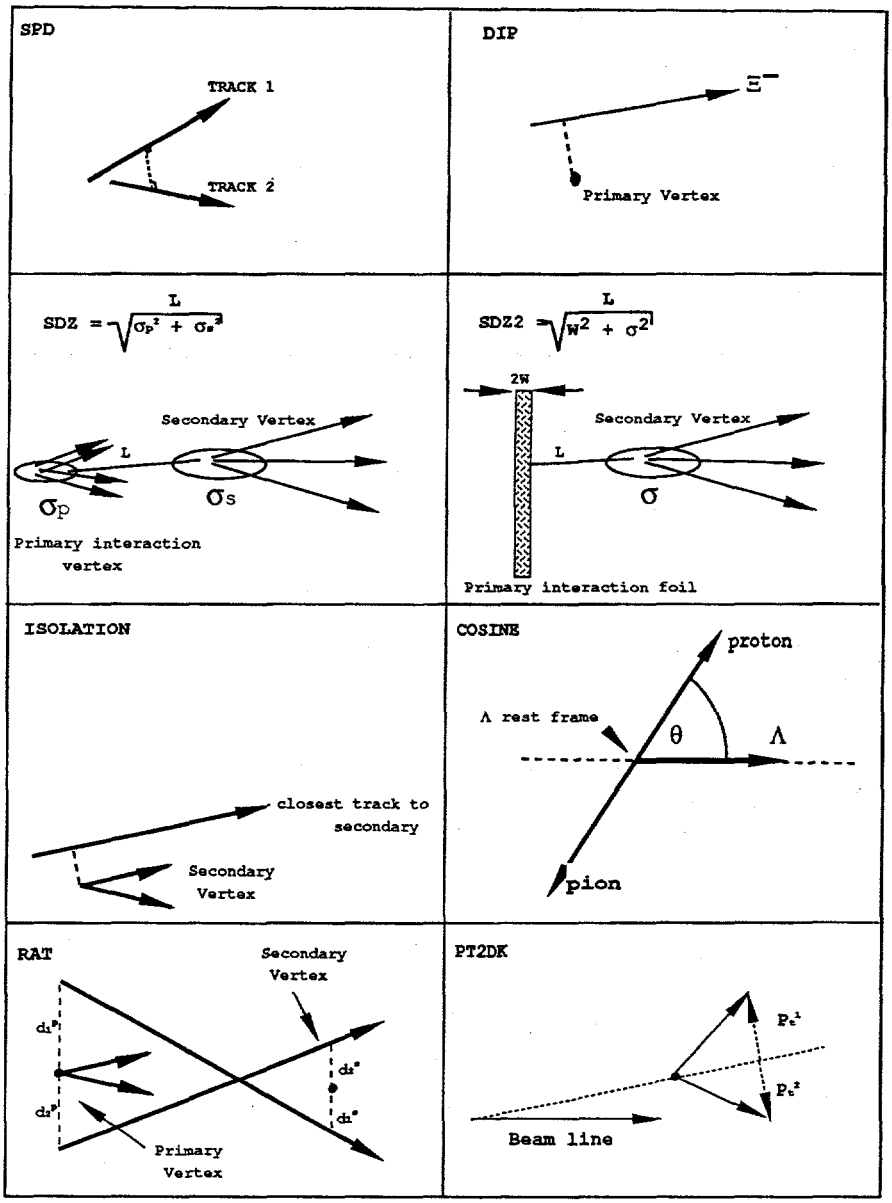

Figure 4.1: Schematic representation of some cuts.

χ^2/n of Secondary Vertex

Reduced χ^2 of vertex from fit, it is obtained by doing a constrained fit of the daughters tracks to a common vertex. This cut is only used for the tracks listed as SMD. It is not possible for Drift chamber tracks due to the lack of their error matrix.

χ^2/n of Tracks

This is a track quality cut calculated as the sum of χ^2/n per degree of freedom of both tracks.

Decay Angle Cut

This cut is used for two-body decays. For Λ^0 decays, for instance, this would be the cosine of the decay angle in the lambda rest frame. Thus, the momentum vector of the proton is calculated in the Lambda rest frame, the angle between this vector and the Lambda momentum vector, projected in this frame, is then calculated. See Figure 4.1

Isolation Cut

Distance of the secondary vertex to the closest non associated track, calculated as the track with shortest impact parameter to the secondary vertex not considering any of the daughter tracks.

Čerenkov cut

Čerenkov identification. This cut is momentum dependent and the set of cuts used can be seen in Table 4.1.[4]

[4]This set of cuts were adjusted by collaboration member Mr. Dave Passmore

Momentum range GeV		Pion probability	Proton probability
0 - 6	>	0.76	0.03
6 - 20	>	0.50	0.25
20 - 36	>	0.95	0.20
36 - 69	>		0.15
69 and above	>		0.04

Table 4.1: **Čerenkov probability cuts.**

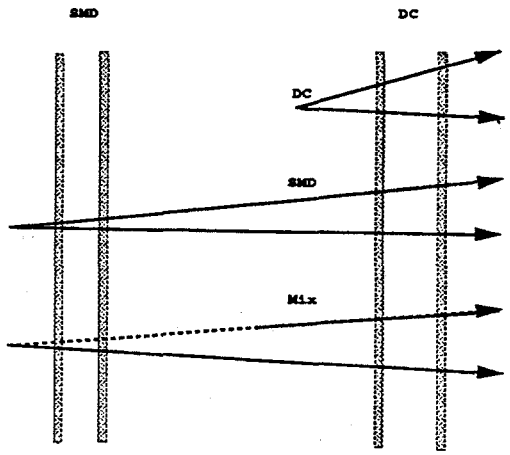

Figure 4.2: Track topologies for lambda search.

4.3 Reconstruction of Lambda Decays

This search for Λ^0 decays involves candidates that decayed anywhere between the target foils and the first magnet. Therefore, two tracks qualify for a lambda decay if *both* tracks have the first bit and any other bit of the array JCATSG set on, that is, they are detected in D1 and any other Drift Chamber detector. This requirement leaves out of the search any tracks for which charge and momentum have not been properly measured, otherwise considered as stubs (JCATSG=1).

Therefore three kinds of search topologies are possible, see Figure 4.2. In the first one, the tracks have both been seen in the SMD detector. This topology contains candidates that are listed on the vertex list (SMD-V), as generated in PASS2 level reconstruction, and others that are not but which may be rescued (SMD-R).

Before the SMD-V search is over, both tracks that served to reconstruct the

		SMD-V	SMD-R	DC	MIX
Distance	<	0.02 cm	0.02 cm	0.4 cm	0.2 cm
χ^2/n secondary	<	2.0	5.00	Not used	Not used
Momentum Ratio	>	3.0	3.0	3.0	3.0
χ^2/n tracks	<	7.00	7.00	7.00	7.00
Decay angle	<	0.99	0.99	0.99	0.99
Isolation	>	0.032 cm	0.032 cm	Not used	Not used
χ^2/n 3-tracks	>	Not used	1.5	Not used	Not used
K short mass range		yes	yes	yes	yes
Čerenkov		yes	yes	Not used	yes

Table 4.2: **Summary of Lambda reconstruction cuts.** These cuts were applied on data contained in the new data set.

lambda candidate were tagged, so that these tracks could not be used in an SMD-R search, Thus in an SMD-R search, the tracks left in the track array list were combined to get a secondary vertex fit with cuts as shown in Table 4.2.

In the second topology, DC, both tracks are observed in the DC detector, only. Finally, in the crossed topology, MIX, where one track comes from SMD and the other from the DC, we expect a small signal or no signal at all, but we will see that it is possible to get some signature here as well. Figure 4.3 shows the response of the spectrometer to the lambda signature.

4.3.1 Lambda Cuts

Apparently, charge is a well measured quantity for all pairs of tracks that meet the requirements discussed above; therefore, a pair must have opposite charge. The adjustable set of cuts is presented in Table 4.2, and a short description of additional cuts is presented below.

Momentum Ratio Cut

Ratio of proton-pion linear momentum. The proton track is assumed to carry most of the momentum of both tracks.

χ^2/n of a Three-track Vertex Cut

The closest track to the secondary vertex is used to calculate the best three-track-vertex having the smallest Chi Square per degree of freedom including the secondary tracks and a third track.

K^0_S Mass Cut

This is the mass difference between the nominal and calculated K^0_S masses. Lambda candidates within this range are discarded.

Z Coordinate Cut

The Z location of the secondary vertex. The allowed values for these cuts are Z < 5.0494 cm. for SMD candidates and Z < 23.825 cm. for DC candidates. There is also an upper limit cut given by the location of the first magnet.

4.3.2 Lambda Histograms

Figure 4.3 shows the response of different sections of the spectrometer to the Λ^0 and K^0_S signature. The last row of histograms in the figure shows some candidates that decayed between the magnets of the spectrometer. The third column of histograms represents K^0_S decays, that also qualify as Λ^0 candidates. All entries, within 10 MeV of the central peak of the K^0_S mass were removed from the Λ^0 sample so that a Λ^0 candidate could not be both a Λ^0 and a K^0_S candidate.

Figure 4.4 show a sample of Lambda decays reconstructed from the vertex list and the Drift Chambers respectively. Monte Carlo studies show that Λ^0 decays detected by the Drift Chamber detector represent the largest sample, therefore only this topology was used for charm baryon search.

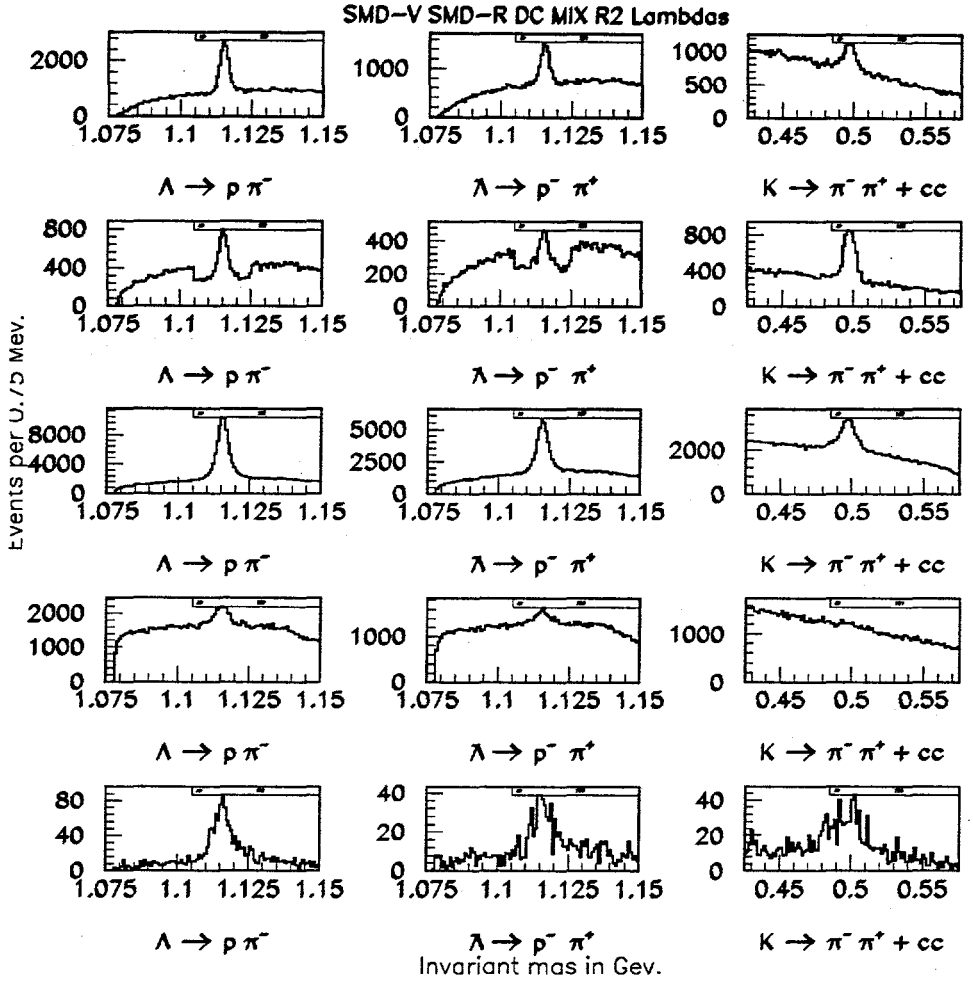

Figure 4.3: Λ^0 and K^0_S decays. From top to bottom, each row shows SMD-V, SMD-R, DC, MIX and Region 2 respectively. The last column shows K^0_S decays. The second row of histograms show a depression close to the Λ^0 peak, which is due to the fact that the data were recorded with the K^0_S mass cut in place. To show the remaining K^0_S signature the cut was relaxed causing the feature. These data were taken from a preliminary pair-strip filter sample.

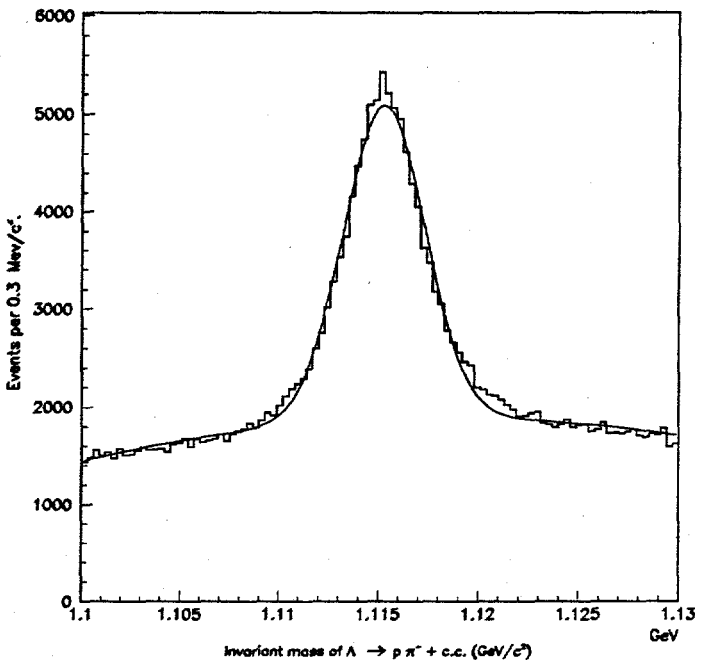

Figure 4.4: **Lambda Decays from Drift Chamber Detector:** Width = 2.1 MeV, Center = 1115 MeV

4.4 The Decay $\Xi_s^- \rightarrow \Lambda^0\pi^-$

Once a Λ^0 candidate has been found a search for a Ξ_s^- is initiated. The decay mode $\Xi_s^- \rightarrow \Lambda^0\pi^-$ demands that we search for a pion candidate track. This candidate has to meet some simple requirements such as not to use either of the Λ^0 decay tracks. It also has to have some definite linear momentum and charge; for this to be true, all pion candidates have to pass through the first magnet of the spectrometer, so that the first bit of array JCATSG has to be set, and JCATSG has also to be greater than 1.

Good[5] Λ^0 and pion candidates are combined to obtain the shortest perpendicular distance between them –required to be less than 5.6 mm– and a secondary vertex position that is required to lie in between the upstream edge of the target, Z = −5.0494 cm. and the Z location of the Λ^0 decay.

Another cut requires that the ratio between the shortest impact parameter of the

[5]Candidates within 2.5σ of the fitted mass.

Ξ_s^- candidate relative to any vertex lying behind the secondary and the z component of the distance between the secondary and the chosen primary be less than 0.016.[6] The full set of cuts used is show in the following list. M and M^* are the measured and the nominal mass respectively.

1. $\left|M(\mathrm{K}_S^0) - M^*(\mathrm{K}_S^0)\right| > 2.5 \times 0.006$ GeV
2. $|M(\Lambda^0) - M^*(\Lambda^0)| < 2.5 \times 0.0021$ GeV
3. JCATSG(π) odd number > 1
4. π track observed in DC detector
5. SPD between Λ and $\pi < 0.68$ cm.
6. $\mathrm{Z}(\Xi_s) < \mathrm{Z}(\Lambda)$
7. -5.0 cm. $< \mathrm{Z}(\Xi_s) < \mathrm{Z}(\mathrm{M1})$
8. $\mathrm{DIP}/\Delta\mathrm{z} < 0.016$
9. $\mathrm{Q}(\pi) = \mathrm{Q}(\pi$ from $\Lambda)$

Contamination by $\Omega_s^- \rightarrow \Lambda^0\mathrm{K}^-$ has been found to be negligible. Figure 4.5 shows cascade decays obtained from around 4 million events. Figure 4.6 shows the cascade signal for the whole data set, by fitting this histogram to the sum of a Gaussian function and a first order polynomial we find a yield of $(8.36 \pm 0.26) \times 10^3$ candidates, at a mass of 1321.1 ± 0.1 MeV/c^2 and width of 2.71 ± 0.07 MeV/c^2.

It has been found that this approach gives impressive Ξ_s^- and $\Xi_s^0(1530)$ yields, see Figure 4.9. However when searching for charm baryons, combinatorial background seems to be a difficulty impossible to overcome.

Another way of searching for Ξ_s^- is to find the actual track left in the Silicon Microstrip Detector. This seems possible because most of the Ξ_s^- decay locations

[6]This cut has been studied and found to be more efficient than the impact parameter alone.

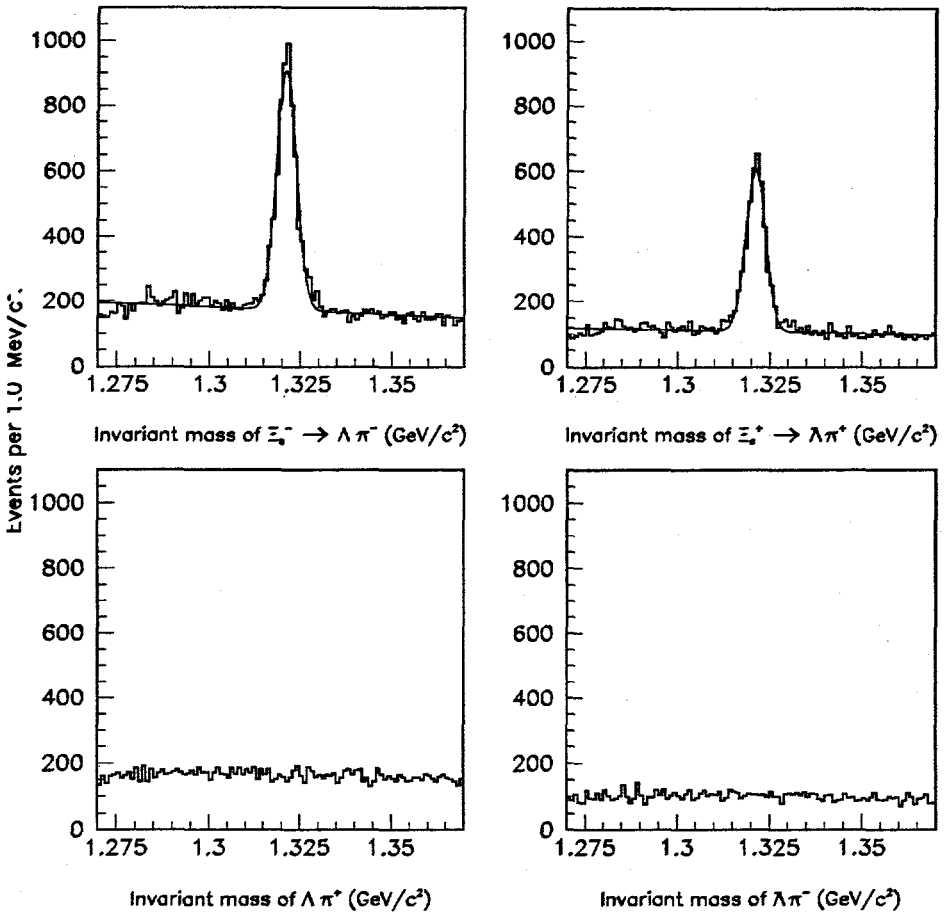

Figure 4.5: **Cascades from Drift Chamber Detector:** The figures at the top show the invariant mass distribution for $\Lambda^0\ \pi^-$ and $\overline{\Lambda^0}\ \pi^+$. The two figures at the bottom show $\Lambda^0\ \pi^+$ and $\overline{\Lambda^0}\ \pi^-$which are not allowed final states for Ξ decays.

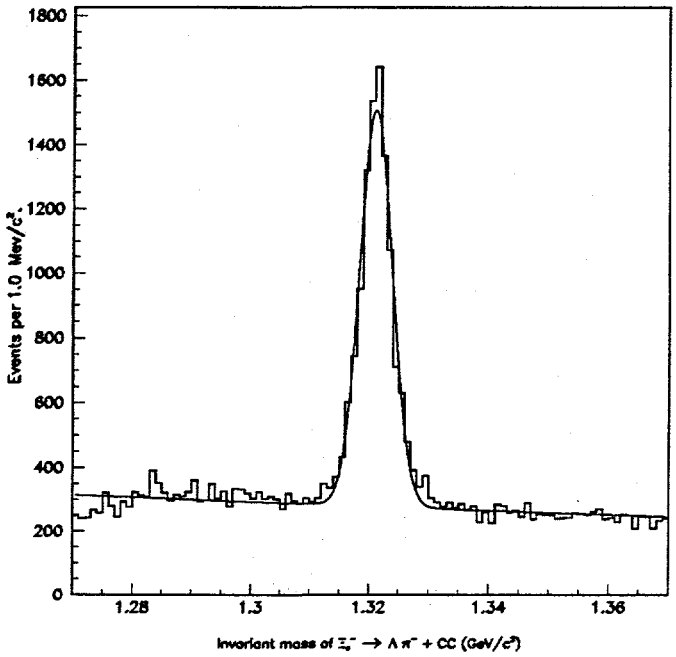

Figure 4.6: **Cascades from Drift Chamber Detector:** The figure shows the invariant mass distribution for $\Lambda\pi^-$ and $\overline{\Lambda}\pi^+$.

occur between the target and the first magnet, see Figure 4.7. Since the last SMD plane is located at 23.80 cm. Ξ_s^- tracks will not be detected by the first Drift Chamber detector, and therefore charge and momentum will not be measured. This kind of track is sometimes called a stub or a 0.5 prong track.

This last strategy is very appealing due to the fact that the actual Ξ_s^- track could be found with a resolution given by the SMD and since the lifetime of charm baryons is expected to be extremely short this track and other tracks detected in the SMD could be used to find a secondary vertex with a reasonable resolution, allowing us to diminish the combinatorial background.

The actual strategy is as follows, see Figure 4.8. First, combine all stubs with a charged track from the Drift chamber detector to form a secondary vertex, this corresponds to the Ξ_s^- track and π^- track of the decay $\Xi_s^- \rightarrow \Lambda^0\pi^-$ respectively. Require that the Λ^0 point to that vertex and its decay Z location be downstream of it. Get the transverse momentum of Λ^0 and the pion with respect to the stub requiring that they be close to a cut value. All of the cuts used for a stub search

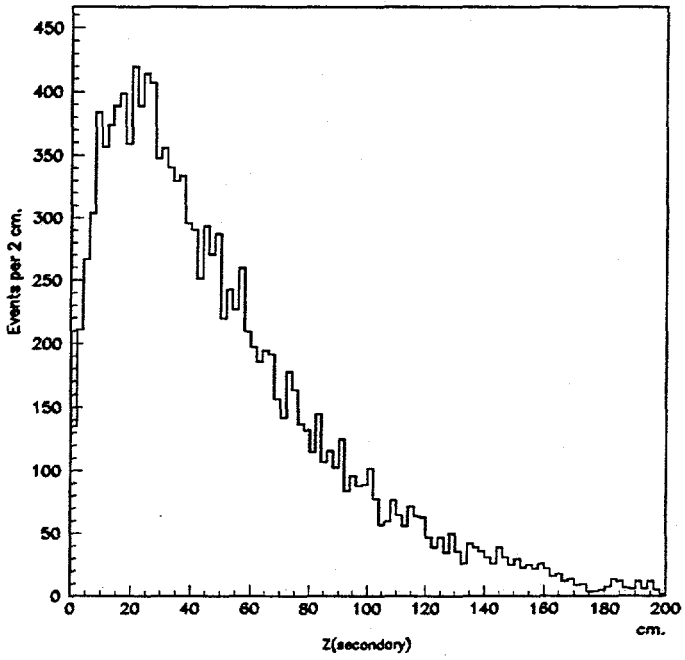

Figure 4.7: **Z location:** This shows that most of the cascade decays occur between the last SMD plane and the first magnet.

are listed in the following table. M and M^* are the measured and the nominal mass respectively.

1. $\left|M(\mathrm{K}^0_S) - M^*(\mathrm{K}^0_S)\right| > 2.5 \times 0.006$ GeV
2. $|M(\Lambda^0) - M^*(\Lambda^0)| < 2.5 \times 0.0021$ GeV
3. $\mathrm{Q}(\pi) = \mathrm{Q}(\pi$ from $\Lambda)$
4. JCATSG(π) odd number > 1
5. π track detected in DC detector
6. SPD between Λ and $\pi < 2.8$ cm.
7. $\mathrm{Z}(\Xi_s) < \mathrm{Z}(\Lambda)$
8. -25.0 cm. $< \mathrm{Z}(\Xi_s) < \mathrm{Z}(\mathrm{M1})$
9. DIP < 0.056 cm.

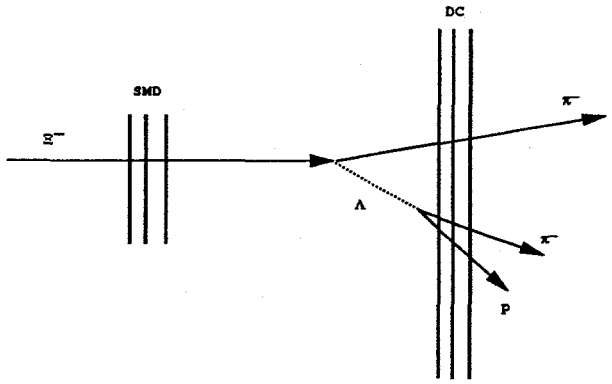

Figure 4.8: **Stub topology search.**

10. LIMP/$\Delta z < 0.025$ cm.[7]

11. $|P_t(\pi^-) - P_t(\Lambda^0)| < 0.016$ GeV

4.5 Cascade Resonant State

In our effort to get charm states decaying into cascades we have also been able to observe the $\Xi_s^0(1530) \rightarrow \Xi_s^-\pi^+$resonant state. This state is obtained by combining all pions selected as SMD tracks with Ξ_s^-. The full sample of these states can be can be seen in Figure 4.9, and a full list of cuts is presented below. M and M^* are the measured and the nominal mass respectively.

1. $|M(\Xi_s^-) - M^*(\Xi_s^-)| < 2.5 \times 0.003$ GeV

2. π detected in SMD

3. π JCATSG odd number > 1,

4. $Q(\pi^+) \times Q(\Xi_s^-) < 0$

5. -5.0 cm. $<$ Z(secondary) $<$ 0.0 cm

[7]LIMP stands for Λ^0 impact parameter with respect to the Ξ_s^- secondary decay point.

6. χ^2/n(Secondary vertex) < 2.5 (*2-track vertex*)

7. χ^2/n(Primary vertex) < 3.0 (*(n+2)-track vertex*)

8. |SDZ| < 1.0

9. DIP < 0.06 cm.

10. $\left|\vec{P}_{\Xi_s^-}\right| / \left|\vec{P}_{\pi^+}\right| > 4.0$

The primary vertex associated with this resonant state has been re-fitted so that both the stub as well as the pion candidate track have been included in the new primary vertex. Although impressive samples have been obtained without using the stub-Ξ_s^- track, the stubs linked to Ξ_s^- tracks has been used in the sample shown here and it provides some degree of confidence when looking for charm states. It is possible to determine some properties of this resonant state by fitting the $\Xi_s^-\pi^+$ mass spectrum to a Breit-Wigner[27] (BW) term and a background (BG) term:

$$\begin{aligned} F_{BG}(m) &= (m-1.47)^{P_2} \times e^{-P_3(m-1.47)^2} \\ F_{BW}(m) &= \frac{m m_R \Gamma_R}{(m^2-m_R^2)^2 + m_R^2\Gamma_R^2} \\ F(m) &= F_{BG} \times (P_1 + P_4 F_{BW}) \end{aligned}$$

In the above expression, m_R and Γ_R are the resonance mass and width respectively. The fitted histogram gives a yield of 596 ± 186 at a mass of 1533.0 ± 0.5. [8] MeV/c^2 and a width of 21 ± 1.7 MeV/c^2.

4.6 The Decay $\Omega_s^- \rightarrow \Lambda^0 K^-$

Since $\Xi_s^- \rightarrow \Lambda^0\pi^-$ decay is topologically equivalent to the decay $\Omega_s^- \rightarrow \Lambda^0 K^-$, it is very straight forward to reconstruct this last mode. It has been noticed that most of

[8] All errors are statistical.

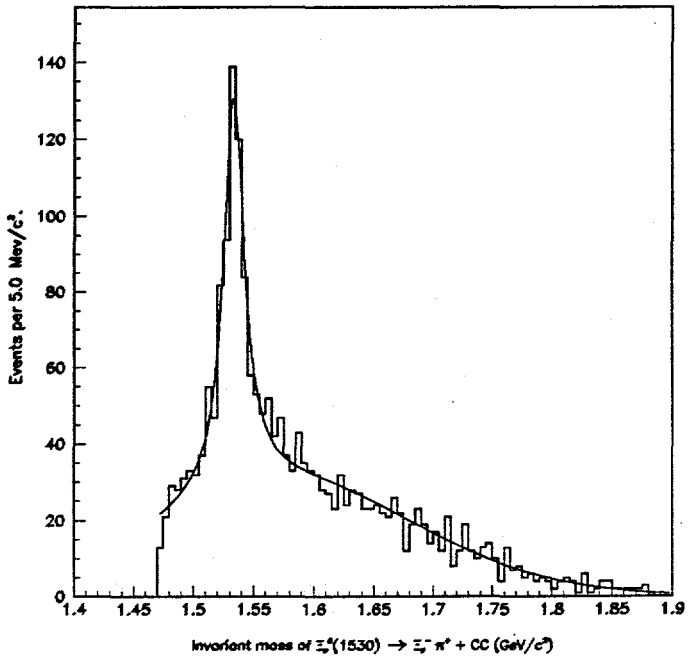

Figure 4.9: **Cascade (1530):** The figure shows $\Xi(1530)$ using a stub track.

the background for this mode comes from either pions or Ξ_s^-, therefore a Čerenkov as well as a Ξ_s^- mass cut have been used to reject the background. The full set of cuts is presented below.

1. $\left|M(\mathrm{K}_S^0) - M^*(\mathrm{K}_S^0)\right| > 2.5 \times 0.006$ GeV
2. $|M(\Lambda^0) - M^*(\Lambda^0)| < 2.5 \times 0.0021$ GeV
3. JCATSG(K) odd number > 1
4. K track must be a DC track
5. SPD between Λ and K < 0.68 cm.
6. $\mathrm{Z}(\Omega_s) < \mathrm{Z}(\Lambda)$
7. -5.0 cm. $< \mathrm{Z}(\Omega_s) < \mathrm{Z}(\mathrm{M1})$
8. DIP < 0.3 cm.
9. $|M(\Xi_s^-) - M^*(\Xi_s^-)| > 2.5 \times 0.003$ GeV

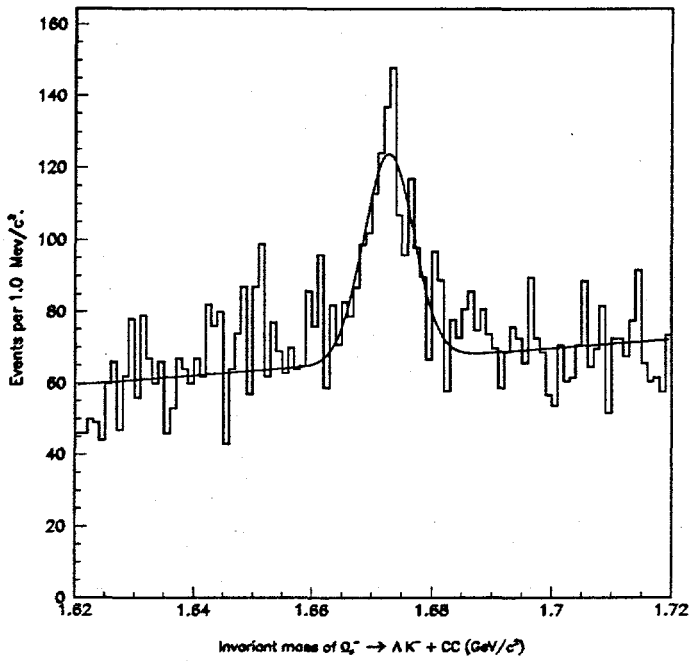

Figure 4.10: **Omega decays:** The figure shows $\Omega_s^- \rightarrow \Lambda^0 K^-$ from Drift Chamber detector.

10. Q(K) = Q(π from Λ)

11. Čerenkov probability for K > 0.13

4.7 The Charm States Ξ_c^0 and Ξ_c^+

After the stub has been successfully pin-pointed, and its momentum reconstructed through the daughters of the Ξ_s^- decay, it is possible to combine this fully reconstructed Ξ_s^- track with other tracks in the SMD detector to seek for charm decays such as $\Xi_c^+ \rightarrow \Xi_s^- \pi^+ \pi^+$ and $\Xi_c^0 \rightarrow \Xi_s^- \pi^+$.

The decay strategy works as follows. The stub track is combined with 2 (for Ξ_c^+) and one (for Ξ_c^0) SMD track(s) to form a secondary vertex. This secondary vertex is required to have a reduced χ^2/n less than 2.5. If any of the pion candidate tracks are consistent with being produced in the primary vertex, the vertex is re-fit without those tracks. The following list details the cuts used to get the charm decay mode $\Xi_c^+ \rightarrow \Xi_s^- \pi^+ \pi^+$.

1. $|M(\Xi_s^-) - M^*(\Xi_s^-)| < 2.5 \times 0.003$ GeV
2. π_i detected in SMD
3. π_i JCATSG odd number > 1,
4. $Q(\pi_i) \times Q(\Xi_s^-) < 0$
5. $Q(\pi_1) \times Q(\pi_2) > 0$
6. -5.0 cm. $<$ Z(secondary) $<$ 0.0 cm
7. χ^2/n(Secondary vertex) < 2.5 (*3-track vertex*)
8. SDZ > 2.5
9. χ^2/n(any 3 tracks) < 3.0
10. DIP < 0.07 cm.
11. $\left|\vec{P}_{\Xi_s^-}\right| / \left|\vec{P}_{\pi(fast)}\right| > 1.0$
12. ISOLATION > 0.002 cm.
13. PT2DK > 0.8 GeV^2

It is important to note the role of the stub track in 2 body decay $\Xi_c^0 \rightarrow \Xi_s^-\pi^+$ since it is probably the only way of getting a reliable vertex. The only alternative to this approach is to use a pseudo Ξ_s^- track which would have had a poorly measured trajectory. For the mode $\Xi_c^0 \rightarrow \Xi_s^-\pi^+$ the cuts are listed below.

1. $|M(\Xi_s^-) - M^*(\Xi_s^-)| < 2.5 \times 0.003$ GeV
2. π detected in SMD
3. π JCATSG odd number > 1,
4. $Q(\pi^+) \times Q(\Xi_s^-) < 0$

5. -5.0 cm. < Z(secondary) < 0.0 cm

6. χ^2/n(Secondary vertex) < 2.5 (*2-track vertex*)

7. SDZ > 2.5

8. DIP < 0.07 cm.

9. ISOLATION > 0.002 cm.

10. PT2DK > 1.0 GeV^2

Figures 4.11 and 4.12 show samples of $\Xi_c^+ \to \Xi_s^-\pi^+\pi^+$ and $\Xi_c^0 \to \Xi_s^-\pi^+$ decays taken from the E769 data set. The width of both signals has been fixed to 10 MeV/c^2 which is a value obtained from Monte Carlo studies. The mass of the Ξ_c^+ decay was fixed to 2466.0 MeV/c^2 which is the current world average[28] and to 2462.0 MeV/c^2 for Ξ_c^0 which is E687 value[11]. Fits have also been done letting the mass and width of the signals to float, the values then obtained are consistent with the current world average. The mass range of the histograms have been extended to 1 GeV around the central peak and a smooth background is observed with signal on top.

The number of events found are 10 ± 4.5 for Ξ_c^+ and 7.9 ± 3.9 for Ξ_c^0. This represents a combined p/K/π production, and therefore in order to get cross sections we would have to break the sample into the different E769 beam types. This final sample is too small to allow separate determination of the cross sections for each beam type. As well see later, in most cases we are only able to set upper limits.

4.7.1 $\Xi_c^+ \to \Lambda^0 K^-\pi^+\pi^+$ Decays

A successful search for the mode $\Xi_c^+ \to \Lambda^0 K^-\pi^+\pi^+$ has also been conducted obtaining a sample of ~24 events. Figure 4.13 shows a mass histogram with these candidates. The list of cuts is presented below.

1. $|M(\Xi_s^-) - M^*(\Xi_s^-)| < 2.5 \times 0.003$ GeV

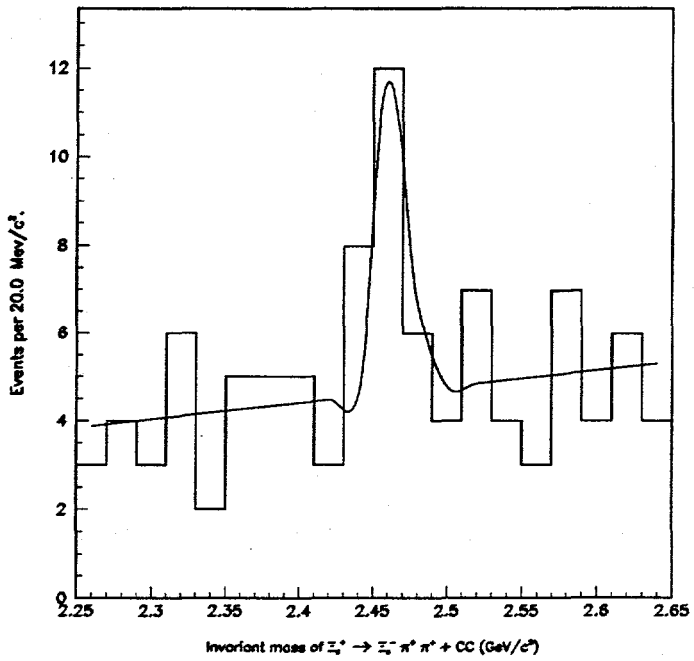

Figure 4.11: $\Xi_c^+ \rightarrow \Xi_s^- \pi^+ \pi^+$ charm state:

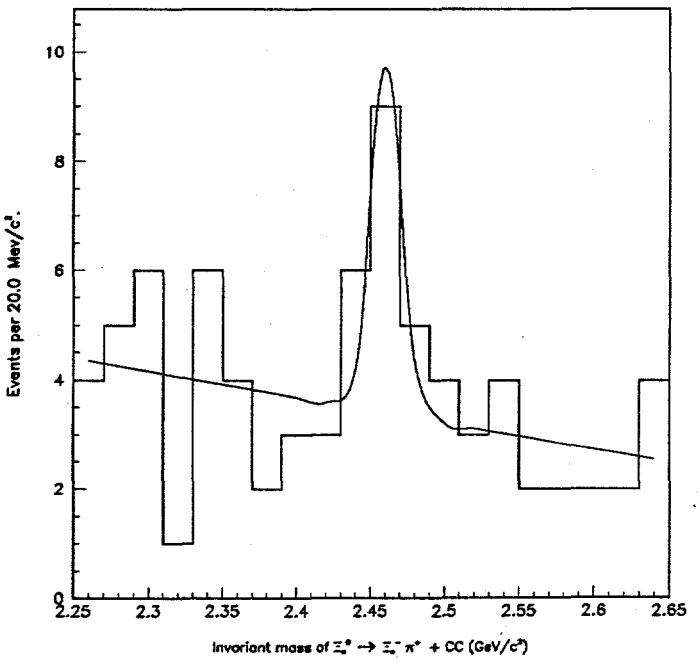

Figure 4.12: $\Xi_c^0 \rightarrow \Xi_s^- \pi^+$ charm state:

2. pions and kaon detected in SMD

3. π,K JCATSG odd number > 1,

4. $Q_\Lambda(\pi^+) = Q(\mathrm{K}^-) < 0$

5. -5.0 cm. $<$ Z(secondary) $<$ 0.0 cm

6. χ^2/n(Secondary vertex) < 2.5 (*2-track vertex*)

7. SDZ > 8.0

8. DIP < 0.07 cm.

9. ISOLATION > 0.005 cm.

10. $\left|\vec{\mathrm{P}}_{\mathrm{K}^-}\right| / \left|\vec{\mathrm{P}}_{\pi(fast)}\right| > 1.0$

11. Čerenkov probability for $\mathrm{K}^- > 0.14$

12. LIMP/$\Delta z < 0.004$ cm.[9]

[9]LIMP stands for Λ^0 impact parameter with respect to the Ξ_c^+ secondary decay point.

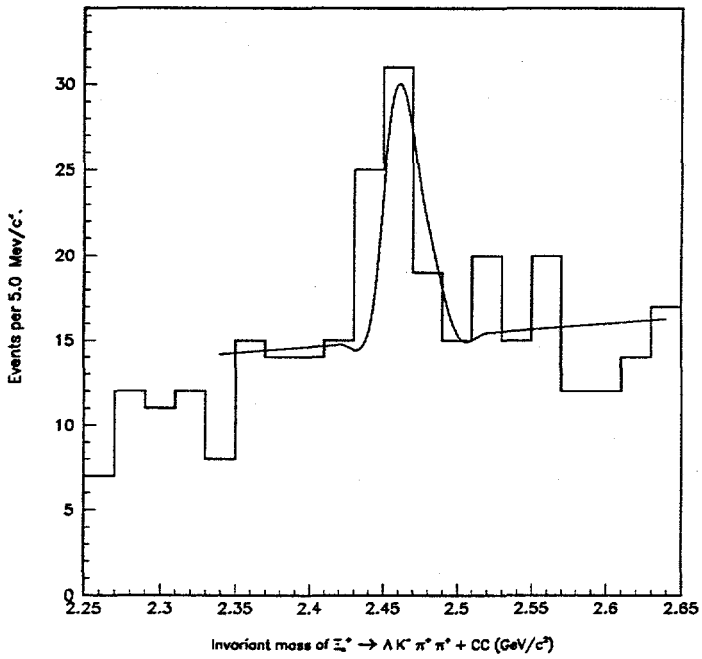

Figure 4.13: $\Xi_c^+ \rightarrow \Lambda^0 K^- \pi^+ \pi^+$charm state.

Chapter 5
Properties of Strange Hyperons

While strange hyperon physics is a topic that has been thoroughly studied for several decades now, this chapter describes a few aspects that might still have some interest.

One of these topics is the atomic mass dependence of the production of Ξ_s^- hyperons. The large E769 data sample should allow us a very precise measurement. Figure 5.1 shows cascade decays sorted by beam type; probabilities for the three different types of beam have been required to be greater than 90%.

Figure 5.2 shows cascade yields versus atomic mass of the target foils. Decays with primary vertex in the Interaction Counter have not been included, but all beam types have. It is possible to get the atomic mass dependence of Ξ_s^- decays if we get the cross-section per nucleon of Ξ_s^-. Unfortunately the data set (pair strip) from which these signals have been extracted is biased to enhance the presence of charmed mesons making the study of systematic errors very complicated. Although an unbiased sample[1] of Ξ_s^- decays has been obtained, early results have shown that in order to do the atomic mass dependence study it is perhaps necessary to do a similar study on pions or kaons.

5.1 Ξ_s^- Lifetime

Although measurements of the Ξ_s^- hyperon lifetime are abundant, it is always a good practice to obtain its value. The technique followed here is a variant of the procedure used in reference [24].

---

[1] From this sample we expect to increase 3 times the number of Ξ_s^- decays.

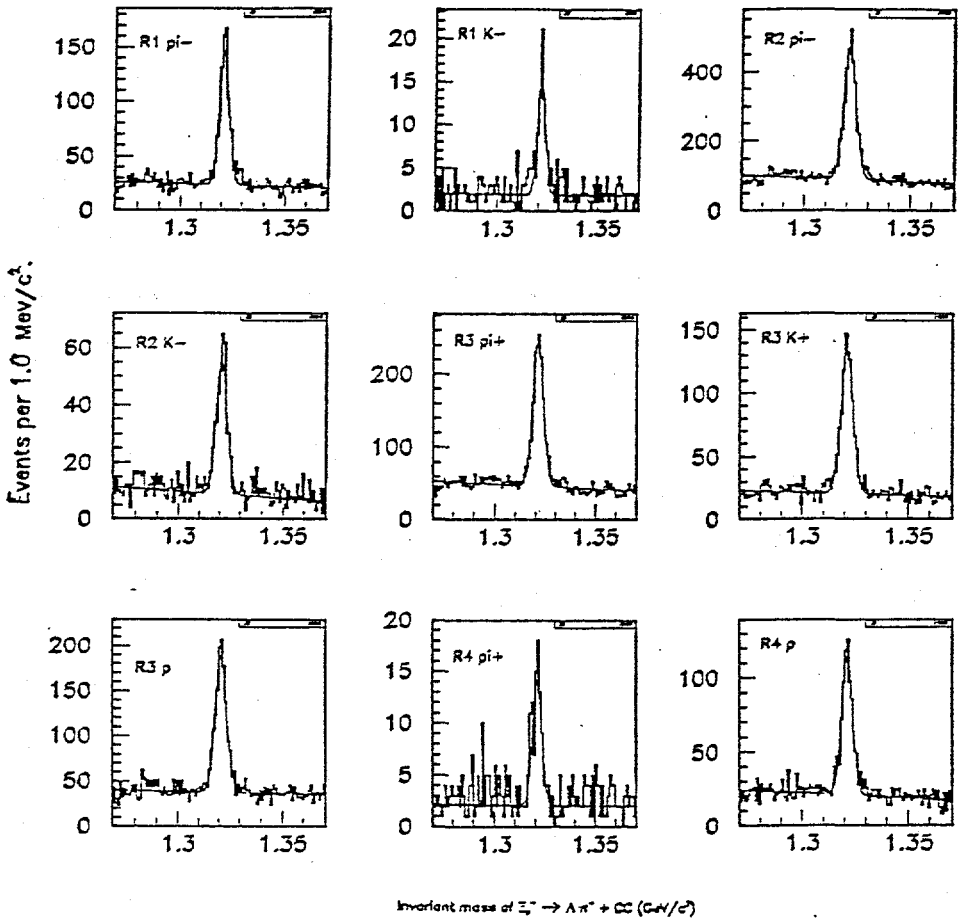

Figure 5.1: Cascade beam types. Ξ_s^- signature from different run regions of the E769 experiment. The histograms also include charge conjugates.

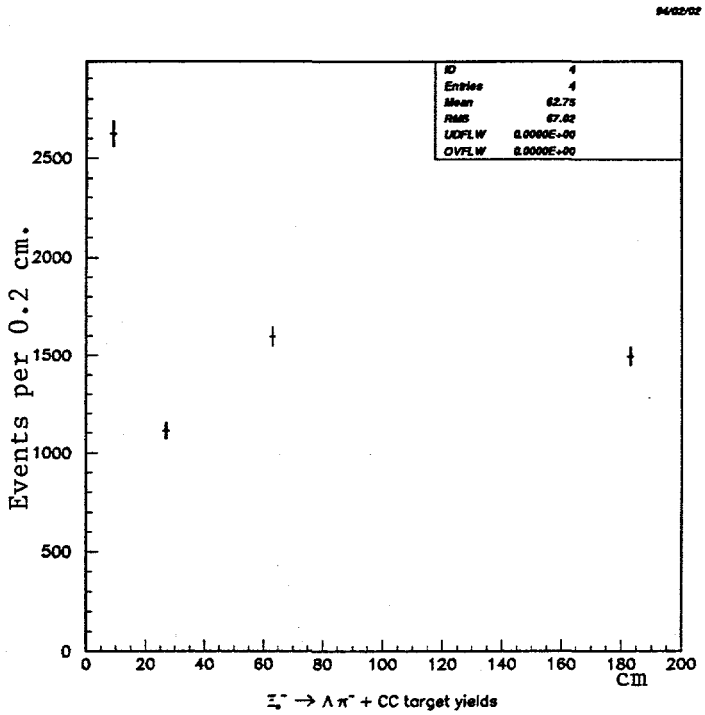

Figure 5.2: **Target type distribution:** The figure shows the number of Ξ_s^- decays as function of the atomic mass A. These histograms are not corrected for acceptance. All beam types and charge conjugates have been combined.

The lifetime of an unstable particle is described by using the exponential decay law

$$\mathrm{N}(t) = \mathrm{N}(0)e^{-\frac{t}{\tau_0}}, \tag{5.1}$$

where $\mathrm{N}(t)$ is the number of particles that lived after a time t. It is simpler to measure ct rather than t where ct is obtained as

$$ct = \frac{\Delta z}{\gamma\beta}$$

with Δz as the distance traveled by the particle in the LAB frame [2] and γ, β are the well known Lorentz factors.

Figure 5.3 shows the distribution of ct for the Ξ_s^- hyperon. Since the detector has less than perfect acceptance the exponential decay law of Equation 5.1 does not represent very well the data in Figure 5.3 and either the formula must be corrected

[2] In a more detailed analysis the reduced lifetime should be calculated, however since this study was intended as quick check of the Ξ_s^- data, the difference between the Z location of the secondary and primary decay was used for Δz.

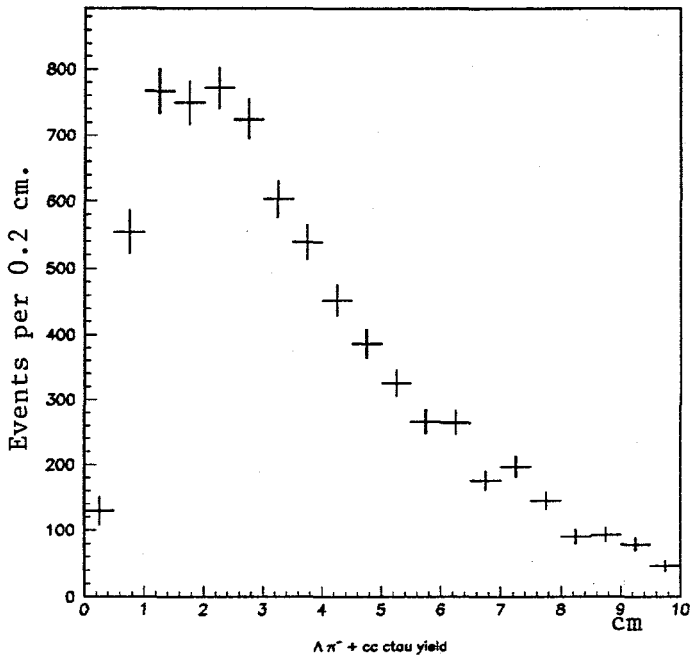

Figure 5.3: Ξ_s^- *ct* distribution: The figure is a background subtracted distribution of Ξ_s^- signal versus lifetime, the background has been subtracted by fitting mass histograms as a function of *ct*. The histogram has been made by expanding ~2 nominal lifetimes in 20 bins.

to represent the observed distribution or the histogram must be corrected to account for all inefficiencies of the detector. In this study the latter technique is implemented.

The corrections needed are done using the Monte Carlo simulation and they arise due to the acceptance of the detector, analysis cut efficiencies, multiple scattering, secondary interactions and hadronic absorption of the hyperon.

The histogram on top in Figure 5.4 is the *ct* distribution taken from the Monte Carlo. A correction for this histogram may be obtained by using the fact that the distribution was generated with an exponential decay law, Equation 5.1, therefore each bin of the histogram must be corrected with a function f_i that measures the deviation from the exponential decay, i.e.

$$f_i(t) = \frac{N_i}{AN_0 e^{-\frac{t_i}{\tau_0}}} \tag{5.2}$$

where N_i is the number of events in the ith bin centered at t_i, τ_0 is the lifetime put in the Monte Carlo generator ($c\tau_0 = 4.78$ cm.), and A is a constant that can be

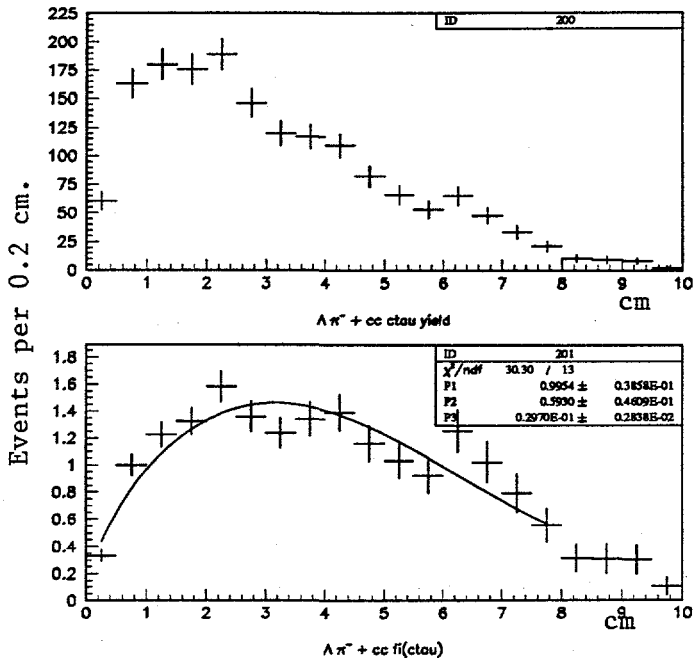

Figure 5.4: Ξ_s^- *ct* **distribution from Monte Carlo:** The histogram on top is the background subtracted *ct* distribution from Monte Carlo simulation data. The histogram in the bottom represents the corrections that are needed to maintain an exponential decay.

obtained by normalizing to 1 a particular bin (ith). Due to low statistics in the first bin the normalization has been carried out in the second bin.

With the distribution $f_i(t)$ it is now possible to correct the real data distribution $n_i(t)$ as

$$n_i'(t) = \frac{n_i(t)}{f_i(t)}.$$

Figure 5.5 shows the histogram in Figure 5.3 corrected for efficiency $f_i(t)$. The first two bins appear low and the last 6 high in the histograms. This effect may be due to low Monte Carlo statistics and detector resolution. A least squares fit to a reduced portion of the histograms gave a $c\tau$ of 4.84±0.49 cm.

Alternatively, the $f_i(t)$ may be fit with an appropriate function and then corrections may be made by a function rather than on a bin by bin basis. A least squares fit of $f_i(t)$ to a function F

$$F(t) = P_1 \times t^{P_2} \times e^{-P_3 t^2} \tag{5.3}$$

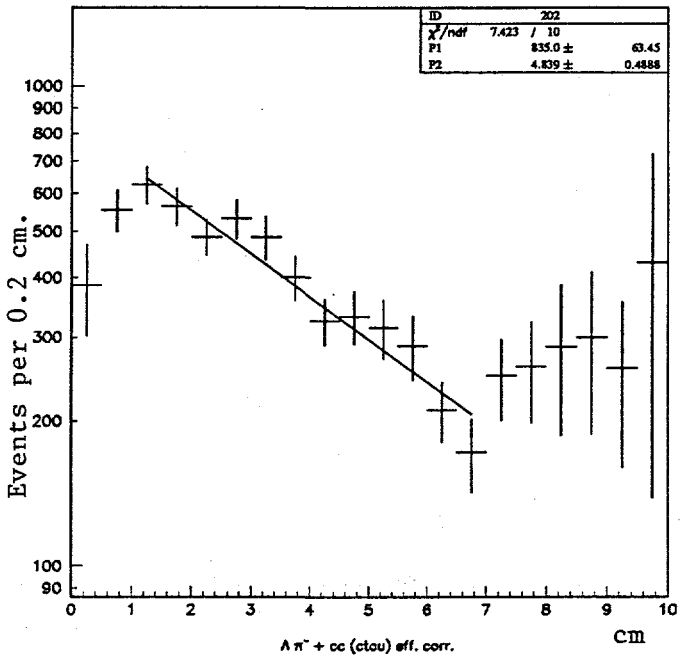

Figure 5.5: **Corrected Ξ_s^- *ct* distribution:** The real data *ct* distribution has been corrected bin by bin with the distribution $f_i(t)$.

gives the parameters $P_1 = 0.9954$, $P_2 = 0.593$ and $P_3 = 0.0297$. Figure 5.6 shows the result of the $F(t)$ correction function. A least squares fit to a reduced portion of the histograms gave a $c\tau$ of 4.64±0.21 cm, in good agreement with the previous value and the world average 4.917±0.045.[28]

5.2 Particle-antiparticle Asymmetry

Recent studies of leading production of $D^{\pm}$ and $D^{*\pm}$ have shown significant deviations from the PQCD predictions from the x_F distribution.[29, 30] A leading charm meson is one with longitudinal momentum fraction, $x_F > 0$, whose light quark (or anti-quark) is of the same type as one of the quarks of the projectile. A similar study is considered here with the Ξ_s^- in which the Asymmetry parameter **A** is defined as

$$\mathrm{A} = \frac{\sigma(\Xi_s^-) - \sigma(\overline{\Xi_s^-})}{\sigma(\Xi_s^-) + \sigma(\overline{\Xi_s^-})},$$

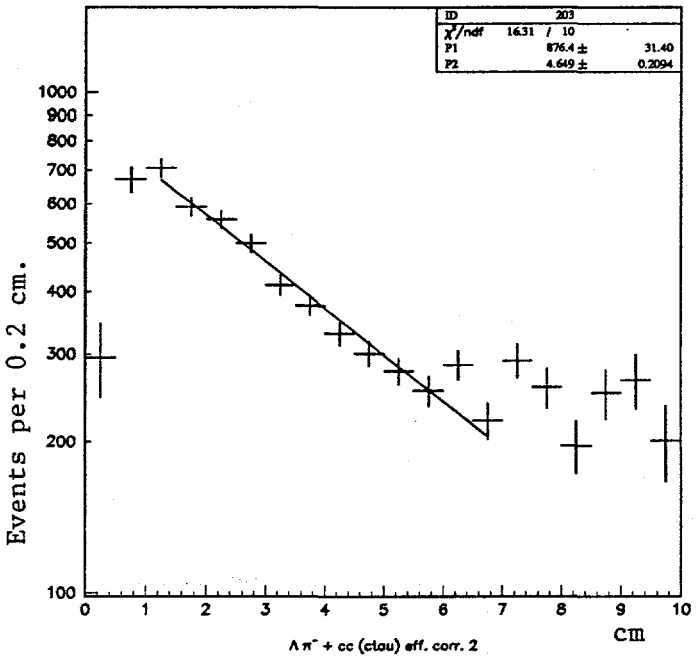

Figure 5.6: **Corrected Ξ_s^- *ct* distribution:** The real data *ct* distribution has been corrected by the function $F(t)$.

where $\sigma(X)$ is the cross section of the hyperon X. [3] Since the asymmetries are involved with ratios of cross sections they can be calculated nearly as precisely by extracting the number of events directly from the mass histograms, then

$$\mathrm{A} = \frac{N(\Xi_s^-) - N(\overline{\Xi_s^-})}{N(\Xi_s^-) + N(\overline{\Xi_s^-})}.$$

This last formula does not involve the experimental acceptance since it is the same for both particles and antiparticles. In other words, the asymmetry from Monte Carlo simulation is consistent with zero. Figure 5.7 shows this effect. The 2 top histograms are the ratio of $N(\Xi_s^-)/N(\overline{\Xi_s^-})$ in the left and the Asymmetry in the right respectively. Both histograms have been obtained from the π^- beam Monte Carlo. The 2 histograms in the bottom are their counterparts but for the π^+ generated Monte Carlo.

The quark content of Ξ_s^- is *ssd* while the beam is composed of:

- $\pi^+(u\bar{d})$, $\overline{\Xi_s^-}$ leading

[3] For other experiments data see reference [25].

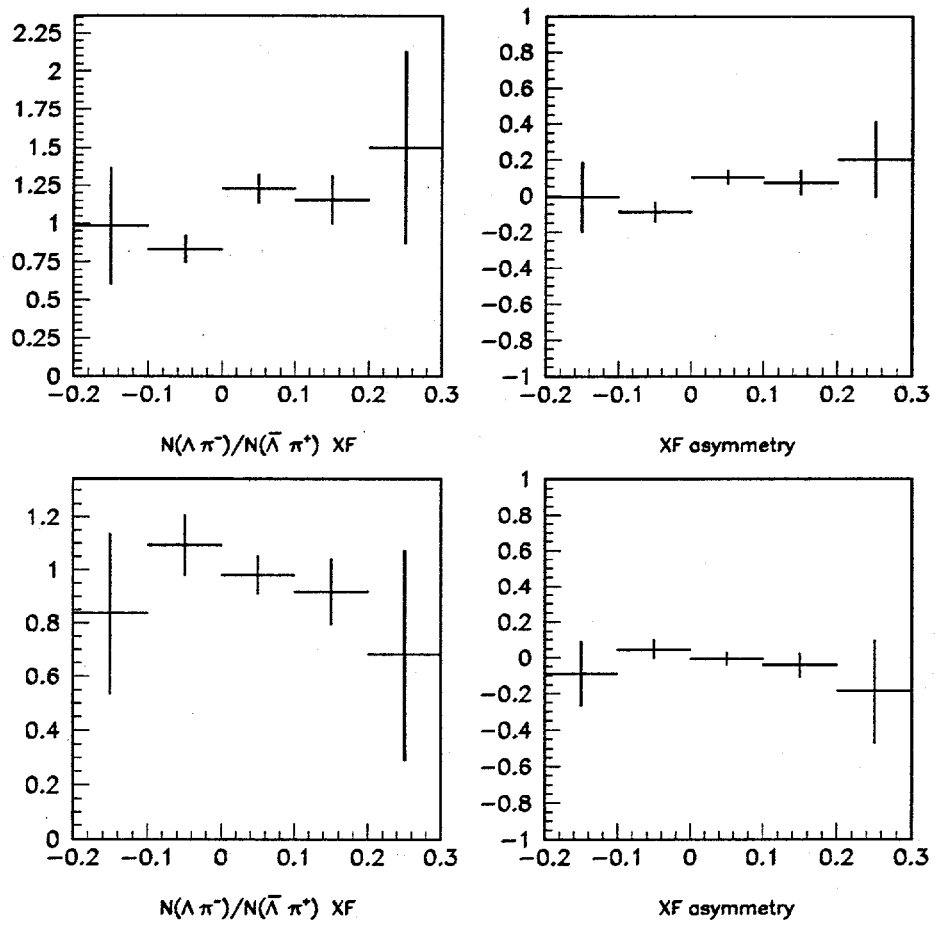

Figure 5.7: **Asymmetry:** The figure shows particle-antiparticle ratio (left) and the Asymmetry (right) as a function of x_F from the Monte Carlo simulation data. The histograms on the top are taken from π^- beam generator and the bottom from π^+.

- $\pi^-(\bar{u}d)$, Ξ_s^- leading
- $K^+(u\bar{s})$, $\overline{\Xi_s^-}$ leading
- $K^-(s\bar{u})$, Ξ_s^- leading
- proton(uud), Ξ_s^- leading

and therefore a strong leading effect must be expected from the Kaon beam data.

Figure 5.8 shows the results for asymmetries of Ξ_s^- hyperon. The data show a trend for increasing asymmetry with x_F in the K^- data and a decreasing one in the K^+ consistent with a leading production effect. The π^- and π^+ data show a slight excess of Ξ_s^- over $\overline{\Xi_s^-}$ for $x_F > 0$. As expected, the proton data show leading effect for Ξ_s^-.

In order to test the hypothesis of constant asymmetry as a function of x_F a comparison of Monte Carlo and real data may be done. A least square fit of the two Monte Carlo histograms gave $\chi^2/n = 1.1$ and $\chi^2/n = 1.3$ for negative and positive data respectively (with 4 degrees of freedom), therefore the Monte Carlo data are consistent with the hypothesis of flat distribution with probabilities 95% and 99% respectively. The real data on the other hand gave $\chi^2/n = 2.2$ and $\chi^2/n = 2.7$ for negative and positive kaon beam data respectively but the probabilities for constant asymmetry have decreased to 70% and 61% respectively.

Figure 5.9 shows the asymmetry parameter as a function of p_t^2. All histograms in this figure are consistent with being flat. The data for π^- π^+ K^-, and proton show excess of Ξ_s^- over $\overline{\Xi_s^-}$ while the K^+ data show the opposite effect.

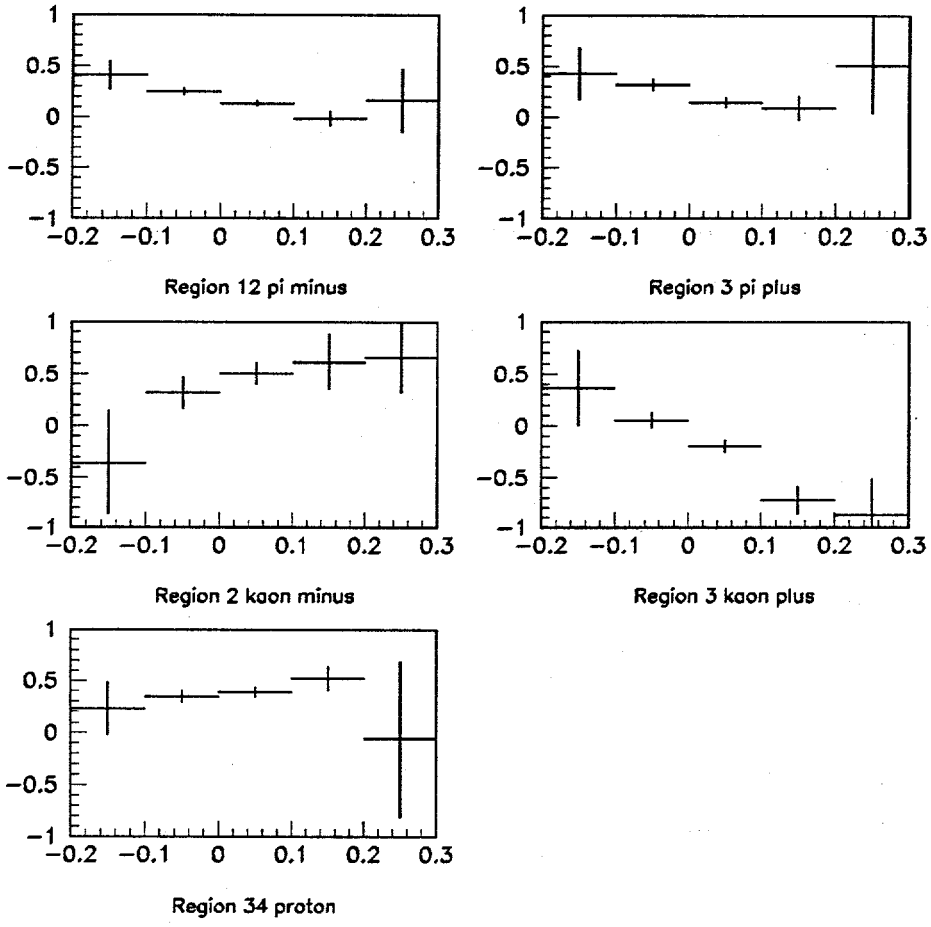

Figure 5.8: **Asymmetry:** particle anti-particle asymmetry as a function of x_F. The horizontal axis is x_F and the vertical axis is the asymmetry as defined above.

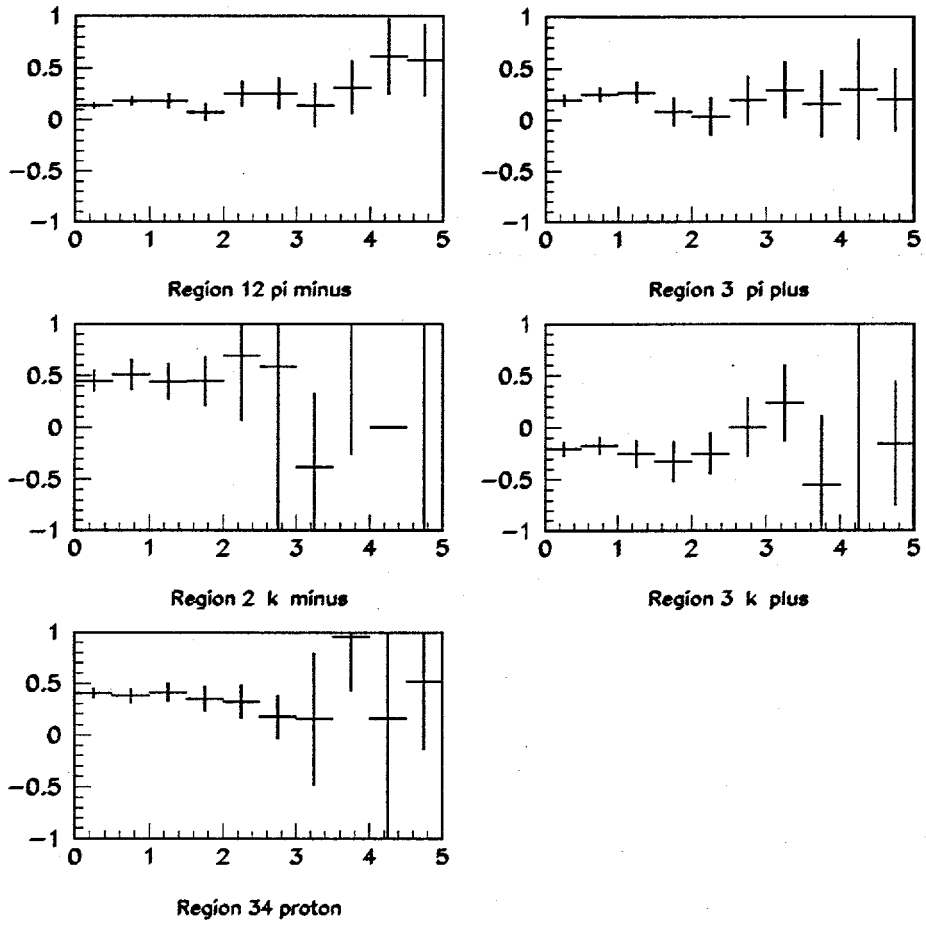

Figure 5.9: **Asymmetry:** particle anti-particle asymmetry as a function of p_t^2. The horizontal axis is p_t^2 and the vertical axis is the asymmetry as defined above and measured in GeV^2.

Chapter 6

The Ξ_c^+ and Ξ_c^0 Cross Sections

It was shown in Section 4.7 that the sensitivity of E769 to $\Xi_c^+ \to \Xi_s^-\pi^+\pi^+$ and $\Xi_c^0 \to \Xi_s^-\pi^+$ states was insufficient to measure separate cross sections for most beam types. In this section the production cross section measurement for $\pi^\pm N \to \Xi_c X$ is detailed, as well as upper limits for all the other beam hadrons.

6.1 The E769 Monte Carlo

In order to determine properties of particles one must know the resolution and efficiency of the apparatus being used. Monte Carlo techniques are commonly used for this purpose. The E769 Monte Carlo simulator was divided into 3 different stages. First, the *Generator* which generated a physical interaction and simulated the passage of the particles produced in the interaction in the detector. The second stage was the *Digitizer* which took the generator output and converted it to the same format as real data. Also at this stage the detector tracking efficiencies were simulated. Finally, the digitizer output was passed to the reconstruction routines just as was the real data.

6.1.1 Event Generation

The Monte Carlo event generator used the JETSET 6.3 framework. The whole event generation was carried out in several stages which are described in the following list

charm pair production In this stage a physical reaction at parton level is simulated. Charm pair production is simulated through the process $g + g \rightarrow c\bar{c}$ or $q + \bar{q} \rightarrow c\bar{c}$. The cross sections for these two processes are calculated according to Nason, Dawson and Ellis[7]. See also [14].

non-charm event Once the $c\bar{c}$ pair is generated the non-charm part of the event is modeled. This part, sometimes also called the underlying event, is the one that simulates a primary interaction between the beam and the target in which non-charm particles are produced. This stage was executed by the package FRITIOF 1.3, which uses an independent string fragmentation model.

fragmentation The $c\bar{c}$ pair is then passed to a fragmentation mechanism. JETSET 6.3 was used to both fragment the pair into hadrons and simulate the decay of unstable particles.

detector simulation At this stage the physical interaction was simulated, and a list of neutral and charged particles obtained together with their momenta, trajectories, and so forth. The rest of the process was to simulate the passage of all these particles through the spectrometer.

6.2 The E769 Cross Section Formulation

From a classical point of view, the total cross section is just the size of the scattered object, i.e. the area of the target in an elastic scattering. The probability that a beam particle *hit* a nucleon of an atom of the target is:

$$\mathcal{P} \equiv \sigma_N \times \rho_n,$$

where σ_N is the cross section of the nucleus and ρ_n is the number of nucleons per unit target-area, and may be conveniently written as

$$\rho_n = \frac{\rho t \mathrm{N}_A}{\mathrm{A}}$$

where ρ, A are the density and atomic mass of target, and N_A is Avogadro's number.

The probability $\mathcal{P}$ can be experimentally determined and may be expressed as the fraction of scattered particles ($\mathcal{O}'$) out of the total number of beam particles ($\mathcal{L}$). Therefore the nuclear cross section may be written as

$$\sigma_N = \frac{A}{\rho t N_A} \times \frac{\mathcal{O}'}{\mathcal{L}}. \tag{6.1}$$

The nuclear cross section Equation 6.1 can be parametrized in terms of the atomic mass, as $\sigma_N = A^\alpha \times \sigma$, where σ is the cross section per nucleon, and α is an experimentally determined coefficient. The value of α used in this study was fixed at 1.0, in accordance with E769 published data for D mesons[31]. This choice for the parameter α is the simplest since there is no data on the atomic mass dependence for charm baryons, and due to the limited statistics in this study it is not possible to get a value using the present data. Then the cross section per nucleon can be written as

$$\sigma = \frac{1}{\rho t N_A} \times \frac{\mathcal{O}'}{\mathcal{L}}. \tag{6.2}$$

The denominator of the first factor, $\rho t N_A$, in Equation 6.2 may be interpreted as the number of nucleons per unit target-area. See section 6.2.1 for more details. Since E769 had 4 different target types, a sum over all of these target types must be carried out.

A problem arises when one tries to determine the incident number of beam particles $\mathcal{L}$, and the number of scattered particles $\mathcal{O}'$. Corrections must be made due to inefficiencies of the detector. The incident number of beam particles must be corrected due to inefficiencies in the identification of the beam particle, and losses due to interactions upstream of the target. On the other hand, only a fraction of the total number of scattered particles is ever detected, let's call this number $\mathcal{O}$, therefore $\mathcal{O}'$ may be written as

$$\mathcal{O}' = \frac{\mathcal{O}}{a}$$

where a is the acceptance and is determined from Monte Carlo simulation.

Equation 6.2 then can be re-written in a generic form as

$$\sigma_{\Xi_c} = \sum_T \left(\frac{1}{\rho t \mathrm{N}_A}\right) \times \frac{\mathcal{O}(\Xi_c)}{a(\Xi_c)\mathcal{L}}.$$

Since the measurement of interest is p/K/π-nucleon cross sections for specific decays of charm-hyperons, namely $\Xi_c^+ \to \Xi_s^-\pi^+\pi^+$ and $\Xi_c^0 \to \Xi_s^-\pi^+$, subscripts must be introduced for σ, $\mathcal{L}$ and a to tag all possible cross section measurements as well as the branching fraction for the specific decay modes. The measurement that will be presented here is finally written as:

$$\sigma_{i\Xi_c^+} \times \mathrm{BR}(\Xi_c^+ \to \Xi_s^-\pi^+\pi^+) = \sum_T \left(\frac{1}{\rho t \mathrm{N}_A}\right) \times \frac{\mathcal{O}_i(\Xi_c^+ \to \Xi_s^-\pi^+\pi^+)}{a_i(\Xi_c^+ \to \Xi_s^-\pi^+\pi^+)\mathcal{L}_i}, \tag{6.3}$$

$$\sigma_{i\Xi_c^0} \times \mathrm{BR}(\Xi_c^0 \to \Xi_s^-\pi^+) = \sum_T \left(\frac{1}{\rho t \mathrm{N}_A}\right) \times \frac{\mathcal{O}_i(\Xi_c^0 \to \Xi_s^-\pi^+)}{a_i(\Xi_c^0 \to \Xi_s^-\pi^+)\mathcal{L}_i}, \tag{6.4}$$

with the index $i = \pi^+, \pi^-, \mathrm{K}^+, \mathrm{K}^-, \mathrm{p}$.

The E769 incident number of beam particles has already been summarized in Table 2.1. The rest of this section is concerned with the determination of the acceptance a_i and the study of systematic errors.

6.2.1 The Nuclear Density

The determination of the nuclear density $\rho t \mathrm{N}_A$ is very simple. The density ρ has been taken from [28] and the thickness from Table 2.3. Table 6.1 summarizes the nuclear densities for all the different target types. The total number of nucleons per cm^2 is $1.6596 \pm 0.0013 \times 10^{24}$.

6.2.2 The Acceptance

The acceptance is determined from running the analysis code in the Monte Carlo Simulation, and is defined as

$$a = \frac{N(accepted)}{N(generated)}, \tag{6.5}$$

	Thickness [mm]	Atomic mass [moles]	density [gr/cm^3]	nuclear-density [cm^{-2}]$\times 10^{24}$
Be	3.629±0.02	9.01	1.848	0.404±0.002
Al	1.261±0.01	26.98	2.7	0.205±0.002
Cu	0.761±0.01	63.55	8.96	0.411±0.005
W	0.383±0.01	183.85	19.3	0.445±0.012
IC	3.175		1.02	0.195

Table 6.1: Nuclear densities of the target.

where $N(accepted)$ is the number of events that pass all the analysis cuts, and $N(generated)$ is the total number of events generated. Equation 6.5 accounts for geometric acceptance and detector efficiencies as they are built into the Monte Carlo simulation program. Some other effects are not simulated and corrections need to be implemented. Here is a list of extra corrections:

Λ^0 Branching fraction The Monte Carlo simulator was forced to generate the mode $\Lambda^0 \rightarrow p\pi^-$ with 100% branching fraction, while the measured ratio is $f = 0.640 \pm 0.005$. The acceptance therefore must be corrected as;

$$a = \frac{N(accepted)}{N(generated)} \times f \tag{6.6}$$

Trigger efficiency The Monte Carlo program did not simulate the trigger and additional corrections must also be included.

The number of accepted events can be easily obtained from the fits to the mass plots of the Monte Carlo data. The acceptance values are summarized in Table 6.2

6.3 Total Cross Sections

All the values necessary to obtain cross section measurements have been described up to now. The measured cross sections for the charm baryons Ξ_c^+ and Ξ_c^0 are summarized in Tables 6.3 and 6.4 respectively. All errors quoted are statistical. As

Mode(beam)	MC yield	$N(generated)$	acceptance
$\Xi_c^+(\pi^-)$	22±5	636716	$2.2\pm0.5 \times 10^{-5}$
$\Xi_c^+(K^-)$	86±10	636716	$8.6\pm1.0 \times 10^{-5}$
$\Xi_c^+(\pi^+)$	5.9±2.6	634887	$0.59\pm0.26 \times 10^{-5}$
$\Xi_c^+(K^+)$	77±9.6	634887	$7.8\pm1.0 \times 10^{-5}$
$\Xi_c^+(p)$	9.1±3.3	634887	$0.92\pm0.3 \times 10^{-5}$
$\Xi_c^0(\pi^-)$	18±4	554041	$2.1\pm0.5 \times 10^{-5}$
$\Xi_c^0(K^-)$	72±9	554041	$8.3\pm1 \times 10^{-5}$
$\Xi_c^0(\pi^+)$	5±2	551086	$0.58\pm0.23 \times 10^{-5}$
$\Xi_c^0(K^+)$	59±8	551086	$6.8\pm0.9 \times 10^{-5}$
$\Xi_c^0(p)$	7.4±2.8	551086	$0.86\pm0.32 \times 10^{-5}$

Table 6.2: Total acceptance for $\Xi_c^+ \rightarrow \Xi_s^-\pi^+\pi^+$and $\Xi_c^0 \rightarrow \Xi_s^-\pi^+$corrected for Λ^0decay branching ratio and trigger efficiency.

Mode(beam)	Events	$\sigma \times$ BR μb
$\Xi_c^+(\pi^-)$	3.6±2.1	1.4±0.8
$\Xi_c^+(K^-)$	1.1±1.4	3.4±4.3
$\Xi_c^+(\pi^+)$	0.1±1.4	0.1±1
$\Xi_c^+(K^+)$	2.1±1.7	2.9±2.4
$\Xi_c^+(p)$	0.7±2.7	0.8±3.1
$\Xi_c^+(\pi^\pm)$	2.7±2.4	0.7±0.6

Table 6.3: E769 Ξ_c^+ forward cross sections ($x_F > 0$). All errors quoted are statistical. The number of events are the result of the fit to the mass histograms.

a result of the limited sample gathered cross sections contain large errors. In most cases the number of events found by the fitter is less than 1. Clearly, in those cases we can only establish limits to the cross sections. Although the statistical errors are large, the combined $\pi^\pm$ cross section for $\Xi_c^+ \rightarrow \Xi_s^-\pi^+\pi^+$is 0.7±0.6 μb and 0.98±0.78 μb for $\Xi_c^0 \rightarrow \Xi_s^-\pi^+$.

6.4 Systematic Errors

All errors quoted up to now are statistical. This section deals with the study of systematic errors. The following list presents some possible sources of systematic

Mode(beam)	Events	$\sigma \times$ BR μb
$\Xi_c^0(\pi^-)$	0.1±1.4	0.04±0.6
$\Xi_c^0(K^-)$	0.93±0.92	3.0±3.2
$\Xi_c^0(\pi^+)$	5.7±2.8	5.6±3.6
$\Xi_c^0(K^+)$	0.1±0.5	0.16±0.79
$\Xi_c^0(p)$	0.1±1.0	0.12±1.2
$\Xi_c^0(\pi^\pm)$	5±3.3	0.98±0.78

Table 6.4: E769 Ξ_c^0 forward cross sections ($x_F > 0$. All errors quoted are statistical. The number of events are the result of the fit to the mass histograms.

errors to the measured cross sections.

1. Target thickness.

2. $\Lambda^0 \rightarrow p\pi^-$branching fraction.

3. The α parameter.

4. Beam normalization.

5. Beam losses in upstream interactions.

6. Effect of the charm baryon mean life in the acceptance.

7. Effect of the charm baryon x_F and p_t^2 simulated distribution in the acceptance.

8. Λ^0 and Ξ_s^- reconstruction efficiencies.

The target thickness introduces a very small error to the cross section. The number quoted for the total number of nucleons per cm. square has already been estimated to be $1.6596 \pm 0.0013 \times 10^{24}$ which introduces an error of $\sim 0.08\%$ in the cross section.

The $\Lambda^0 \rightarrow p\pi^-$branching fraction on the other hand has been accurately measured as 0.640±0.005[28], which introduces an error of $\sim 0.8\%$.

Mode	τ Statistical Uncertainty	σ change
Ξ_c^+	$\mp 23\%$	$^{+21}_{-18}\%$
Ξ_c^0	$\mp 21\%$	$^{+2.2}_{-2.6}\%$

Table 6.5: Change in the cross section by altering the charm baryon mean life in the generator. The statistical error has been taken from reference [10].

The beam normalization errors have been estimated as 2% for π^- beam. The upstream beam correction accounts for an increase of 0.2% in the cross section. See reference [14].

Monte Carlo Mean Life

The Monte Carlo program simulated the charm baryon according to a list of parameter presumed known about the particle. One of them is the mean life which was set at 3.0×10^{-13} s for Ξ_c^+, and 8.2×10^{-14} s for Ξ_c^0. Since this parameter is known within 20% statistical error it introduces a systematic error in the acceptance. The estimates for these errors are summarized in Table 6.5 and a more detailed discussion of the procedure is given in Appendix B.

x_F and p_t^2 Simulated Distribution

The cross section is usually parametrized as:

$$\frac{d^2\sigma}{dx_F dp_t^2} = A(1 - |x_F|)^n e^{-bp_t^2}.$$

The parameters n and b are determined experimentally. The E769 Monte Carlo generates events and this parametrization can be used to fit the simulated data. An uncertainty arises in the total cross section due to the error in the parameters. Unfortunately, there are no experimental measurements of these parameters, leaving

the total cross section quoted in this document with an undetermined systematic error.

Λ^0 and Ξ_s^- Reconstruction Efficiencies

The detector tracking efficiencies were simulated in the Monte Carlo generator. It is therefore necessary to look in the reconstruction efficiencies for discrepancies with the real data. One way of determining this, is to study reconstruction efficiencies as a function of lifetime.

In Chapter 5 the study of Ξ_s^- lifetime was presented. From this study we see no major discrepancies between the Monte Carlo and the real data.

Similar studies for Λ^0 are not finalized at this moment but no major differences are expected.

The SDZ Cut

Another source of systematic error, may be the fact that one of the analysis cuts imposed to get the sample of charm baryon states is less restrictive than the pair-strip filter cut. That cut is the SDZ cut. The pair strip filter required a cut at SDZ > 6, while the charm baryon analysis required a cut at SDZ > 0 for Ξ_c^0 and SDZ > 2.5 for Ξ_c^+. A study was done in order to determine whether the charm baryon passed or not the filter. This study shows that 74% of the time one or both pion tracks of the $\Xi_c^+ \rightarrow \Xi_s^-\pi^+\pi^+$ decay passed the filter, while only 23% of the time the pion track of the decay $\Xi_c^0 \rightarrow \Xi_s^-\pi^+$ passed the filter. The reason for this low rate in the case of Ξ_c^0 is due to the fact that the pair-strip filter requires two tracks for the test, and $\Xi_c^0 \rightarrow \Xi_s^-\pi^+$ can only provide with one track (π^-).

6.5 Final Summary

E769 has gathered a small sample of charm baryons Ξ_c^+ and Ξ_c^0. This sample allows us to set upper limits only for the cross sections. The following table shows these limits.

Mode(beam)	$\sigma \times$ BR μb
$\Xi_c^+(\pi^-)$	< 3.1
$\Xi_c^+(K^-)$	< 12
$\Xi_c^+(\pi^+)$	< 2.2
$\Xi_c^+(K^+)$	< 4.4
$\Xi_c^+(p)$	< 7.4
$\Xi_c^0(\pi^-)$	< 0.74
$\Xi_c^0(K^-)$	< 10.0
$\Xi_c^0(\pi^+)$	< 9.1
$\Xi_c^0(K^+)$	< 3.0
$\Xi_c^0(p)$	< 2.4

Table 6.6: E769 Ξ_c^+ and Ξ_c^0 limiting cross sections at 90% confidence level.

If π^+ and π^- cross sections do not differ much, a cross section limit for the combined $\pi^\pm$ beam may be obtained. These measurements; quoted directly from the data with statistical and systematic error and also as upper limits, are shown in the following table:

Mode(beam)	$\sigma \times$ BR μb
$\Xi_c^+(\pi^\pm)$	$0.66 \pm 0.60^{+0.14}_{-0.12}$
$\Xi_c^+(\pi^\pm)$	< 1.4
$\Xi_c^0(\pi^\pm)$	$0.98 \pm 0.78 \pm 0.02$
$\Xi_c^0(\pi^\pm)$	< 1.6

Table 6.7: E769 Ξ_c^+ and Ξ_c^0 forward cross section. The cross section limits are at 90% confidence level. The errors quoted are statistical first and systematic second.

These limits have been obtained assuming an atomic mass dependence of $\alpha =$

1.0. This assumption cannot be tested at this moment and a future generation of charm baryon experiments will have to settle its validity. No measurements of branching ratio are available at this moment, making the determination of the cross section impossible. However, if these states are not too different than Λ_c^+, we may assume that the typical low branching ratio is about the same, that is, ~3%. Since $\sigma \times \mathrm{BR} \lesssim 1.0 \mu\mathrm{b}$, then the cross section for Ξ_c^+ or Ξ_c^0 is $\lesssim$ 33 μb, a value not at all inconsistent with the QCD prediction of $\lesssim$ 50 μb for σ_{cc}.

E769 has also gathered large samples of Ξ_s^-, Ω_s^- and $\Xi_s^0(1530)$ states. This large sample should be used to study the atomic mass dependence and also the leading particle effect. Preliminary studies indicate a strong leading effect for Ξ_s^- with kaon beam.

Appendix A
Example of Choosing a Cut

As an example of choosing a cut, see Figure A.1. In this case a cut for the variable $DIP/\Delta z$ needs to be found. Distributions of signals (s_i) and backgrounds (s_i) can be determined as explained in Chapter 4. The significance of the signal, $\mathcal{S}_i$, is then determined as:

$$\mathcal{S}_i = \sum_1^i \frac{s_i}{\sqrt{s_i + s_i}}.$$

with i running over the whole range ploted. The limits of the sum have been set according to the range where the signal is expected to group, that is, most of the signal is at low $DIP/\Delta z$ while the background might be in the whole range.

Clearly, from the significance histogram a cut at $\log_{10} DIP/\Delta z = -2.1$ must be set, that is, $DIP/\Delta z \leq 0.0079$. The histogram at the bottom shows the effect of the cut.

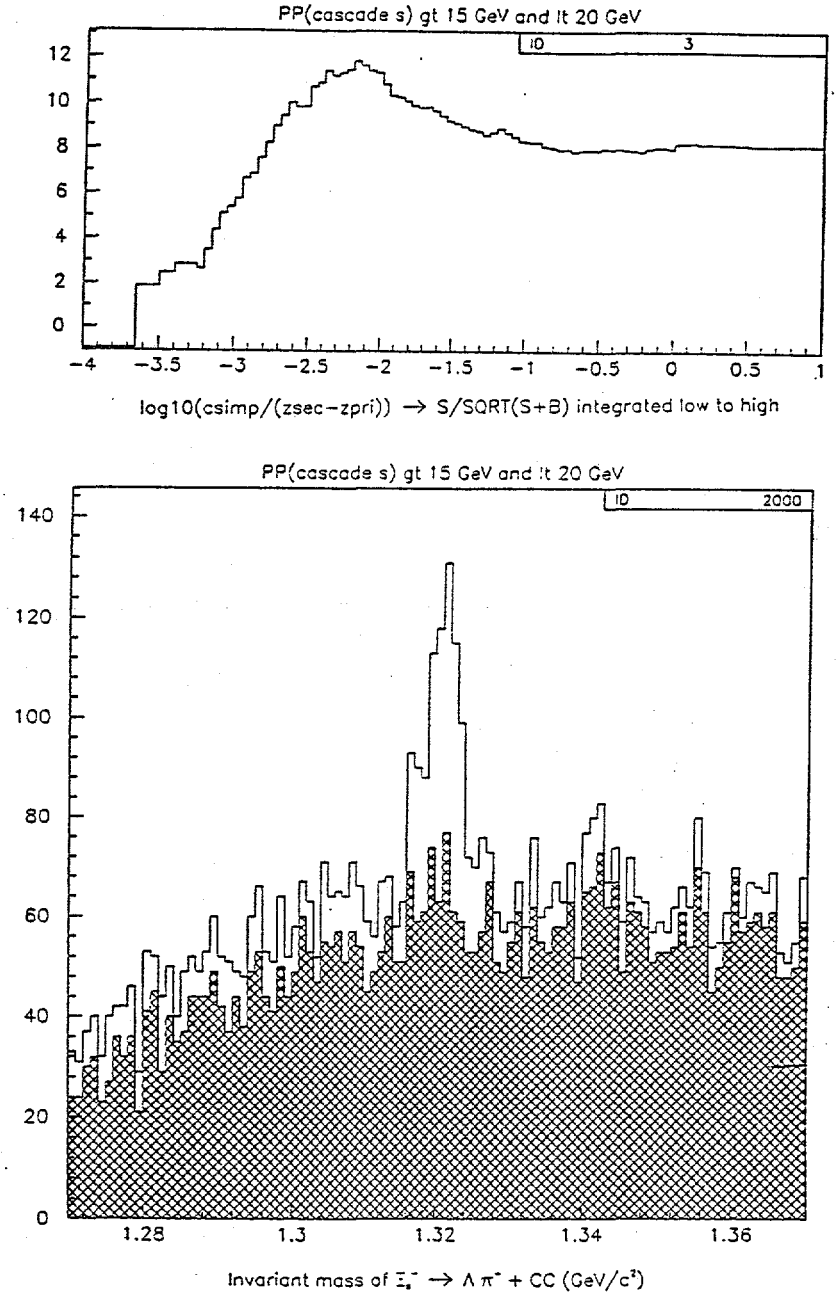

Figure A.1: The histogram on top show the significance of the signal as a function of $\log_{10} DIP/\Delta z$. The logarithm has been introduced only because of the long range of $DIP/\Delta z$. The histogram below shows the effect of setting the cut at $DIP/\Delta z \leq 0.0079$. The shaded region represents the rejected events.

Appendix B
Mean Life Weighting Function.

In order to study the effect in the acceptance due to the lifetime, distribution of the Monte Carlo simulation, a weighting procedure has been used.

The lifetime of the Ξ_c charm baryon for example is known with 20% measurement errors. Since the lifetime distribution is generated according to a decaying exponential, a finely binned histogram of the generated lifetime should fit to function

$$G(t) = G(0)e^{-t/\tau},$$

where τ is the mean life. Once the generated events pass through the detector and analysis cuts, a lifetime histogram looks completely different and the exponential decay might not in general fit the histogram. Let us call this function $r(t)$. The accceptance is then defined as

$$a(t) \equiv \frac{r(t)}{G(t)}.$$

The acceptance, $a(t)$ is a property of the detector itself and if events are generated using a different mean life constant τ', then one would expect

$$\begin{aligned} G'(t) &= G'(0)e^{-t/\tau'} \\ G'(t) &= \frac{r'(t)}{a(t)} \end{aligned}$$

Therefore, $r'(t)$ can be written as

$$r'(t) = W(t) \times r(t)$$

where $W(t)$ is a weighting function and is written as

$$W(t) = \frac{\tau}{\tau'} \times \frac{e^{-t/\tau'}}{e^{-t/\tau}},$$

and the constant factor $G'(0)$ has been evaluated assuming that the total number of generated events is the same for both distributions, that is,

$$\int_0^\infty G(t)dt = \int_0^\infty G'(t)dt$$

References

[1] M. Gell-Mann, *Phys. Lett.* **8** 214 (1964).

[2] G. Zweig, CERN Report, 8182/TH-401 (1964).

[3] J. A. Appel, *Annu. Rev. Nucl. Part. Sci.* **42** 367 (1992).

[4] M. Gluck, D. Sivers, E. Reya, *Phys. Rev.* **D17** 2324 (1978).

[5] B. L. Combridge, *Nucl. Phys.* **B151** 429 (1979).

[6] J. Babcock, D. Sivers, S. Wolfram, *Phys. Rev.* **D18** 162 (1978).

[7] P. Nason, S. Dawson, R. K. Ellis, *Nucl. Phys.* **B303** 607 (1988).

[8] W. Beenakker, W. L. Van Neerven, *Nucl. Phys.* **B351** 507 (1991).

[9] D. W. Duke, J. F. Owens, *Phys. Rev.* **D30** 49 (1983).
J. F. Owens, *Phys. Rev.* **D30** 943 (1983).

[10] P. S. Barlag,*et al.*, *Phys. Lett.* **247** 113 (1990).
P. S. Barlag,*et al.*, *Phys. Lett.* **236** 495 (1990).
P. S. Barlag,*et al.*, *Phys. Lett.* **233** 522 (1989).

[11] P. L. Fabretti,*et al.*,E687, *Phys. Rev. Lett.* **70** 2058 (1993).
P. L. Fabretti,*et al.*,E687, *Phys. Rev. Lett.* **70** 1381 (1993).

[12] Christopher Darling, *The Beauty and Charm Production Cross Sections in 250 GeV/c π^+-Nucleon Interactions.* Ph.D. Thesis, Yale University, New Haven, Connecticut, 1993.

[13] Robert Jedicke, *Flavor Dependence of Hadroproduced Charm-Strange Mesons.* Ph.D. Thesis, University of Toronto, Toronto, Canada, 1991.

[14] Colin Gay, *The Charm Cross Section and Atomic Number Dependence in π^-N Collisions.* Ph.D. Thesis, University of Toronto, Toronto, Canada, 1991.

[15] Richard C. Fernow, *Introduction to Experimental Particle Physics.* 1st edition, Cambridge University Press, Cambridge, UK, 1986.

[16] D. Errede, *et al.*, *NIM* **A309** 386 (1991).

[17] H. M. Rosenberg, *The Solid State.* 3rd edition, Oxford University Press, New York, 1989.

[18] J. C. Anjos, *et al., Proceedings of the III ICFA School on Instrumentation in Elementary Particle Physics.* 1st edition, World Scientific Publishing, Singapore, 1992.

[19] John D. Jackson, *Classical Electrodynamics.* 2nd edition, John Wiley & Sons, New York, 1975.

[20] Bartlett, *et al., NIM 55-75* **A260** 55 (1987).

[21] Some of this information has been collected by personal e-mail, collaboration meetings with Austin Napier, Jeff Appel, Paul Karchin, Marleigh Sheaff, and also blueprints of the electronics of E769.

[22] Steve Bracker, *An Amateur's Guide to the E-769 Trigger Logic* DA's account document TPL VAX Cluster, TPL, 1987.

[23] Sandra F. Amato, *Produção do $D^{*\pm}$ em colisões Hadron-núcleo á 250 GeV, observado no modo de decaimento $D^0\pi^\pm$, $D^0 \rightarrow K^\mp\pi^0$.* Ph.D. Thesis, Centro Brasileiro de Pesquisas Físicas, Rio de Janeiro, Brasil, 1992.

[24] J. R. Raab *et al.*, E691, *Phys. Rev. D* **37** 2391 (1988).

[25] E. Balea *et al., Nuc. Phys.* **B150** 345 (1979).
I. V. Ajinenko *et al., Nuc. Phys.* **B176** 51 (1980).
S. Mikocki *et al., Phys. Rev D* **34** 42 (1986).

[26] Don Summers, *A study of the Decay $D^0 \rightarrow K^-\pi^+\pi^0$ in High Energy Photoproduction*, Ph. D. Thesis, University of California, Santa Barbara, (1984)

[27] C.C. Chang, et al., *Diffractive production of $K^0_s K^0_s \pi^+\pi^-\pi^-$ in $\pi^- N$ interactions at 200 GeV/c* Phys. Rev. D **29**,1888. (1984).

[28] Particle Data Group, K. Hikasa *et al.*, Phys. Rev. D **45**, No. 11, Pt.II (1992)

[29] G.A. Alves et al., E769 collaboration, *Enhanced Leading Production of $D^\pm$ and $D^{*\pm}$ in 250 GeV/c $\pi^\pm$-nucleon Interactions.* Phys. Rev. Lett. **72**, 812-815. 1994.

[30] M. Adamovich et. al., WA82 collaboration, . Phys. Lett. **B305**, 402. 1993.

[31] G.A. Alves, et. al., E769 collaboration, *Atomic mass dependence of $D^\pm$, D^0, and $\bar{D}^0$ production in 250 GeV/c $\pi^\pm$-nucleon interactions*, Phys. Rev. Lett, **70** 722. 1993.